









Chemical abundances and ionizing mechanisms in the star-forming double-ring of AM 0644-741 using MUSE data

V. M. A. Gómez-González , ¹★ Y. D. Mayya , ² J. Zaragoza-Cardiel , ^{2,3,4} G. Bruzual , ⁵ S. Charlot , ⁶ G. Ramos-Larios , ^{7,8} L. M. Oskinova, ¹ A. A. C. Sander ⁹ and S. Reyero Serantes ¹

¹Institute for Physics and Astronomy, Universität Potsdam, Karl-Liebknecht-Str. 24/25, D-14476 Potsdam, Germany

²Instituto Nacional de Astrofísica, Óptica y Electrónica, Luis Enrique Erro 1, 72840 Tonantzintla, Puebla, Mexico

³Consejo Nacional de Humanidades, Ciencias y Tecnologías, Av. Insurgentes Sur 1582, 03940 Mexico City, Mexico

⁴Centro de Estudios de Física del Cosmos de Aragón (CEFCA), Plaza San Juan, 1, E-44001 Teruel, Spain

⁵Instituto de Radioastronomía y Astrofísica, UNAM Campus Morelia, Apartado postal 3-72, 58090 Morelia, Michoacán, Mexico

⁶CNRS, Institut d'Astrophysique de Paris, Sorbonne Université, UMR7095, F-75014 Paris, France

⁷Instituto de Astronomía y Meteorología, CUCEI, Univ. de Guadalajara, Av. Vallarta 2602, Arcos Vallarta, 44130 Guadalajara, Mexico

⁸CUCEI, Universidad de Guadalajara, Blvd. Marcelino García Barragán 1421, 44430 Guadalajara, Jalisco, Mexico

⁹Zentrum für Astronomie der Universität Heidelberg, Astronomisches Rechen-Institut, Mönchhofstr. 12-14, D-69120 Heidelberg, Germany

Accepted 2024 February 20. Received 2024 February 20; in original form 2023 April 10

ABSTRACT

We present the analysis of archival Very Large Telescope Multi-Unit Spectroscopic Explorer observations of 179 H II regions in the star-forming double-ring collisional galaxy AM 0644-741 at 98.6 Mpc. We determined ionic abundances of He, N, O, and Fe using the direct method for the brightest H II region (ID 39); we report $\log(\frac{N}{O}) = -1.3 \pm 0.2$ and $12 + \log(\frac{O}{H}) = 8.9 \pm 0.2$. We also find the so-called ‘blue-bump’, broad He II $\lambda 4686$, in the spectrum of this knot of massive star formation; its luminosity being consistent with the presence of ~ 430 Wolf–Rayet (WR) stars of the nitrogen late-type. We determined the O abundances for 137 H II regions using the strong-line method; we report a median value of $12 + \log(\frac{O}{H}) = 8.5 \pm 0.8$. The location of three objects, including the WR complex, coincide with that of an Ultra Luminous X-ray source. Nebular He II is not detected in any H II region. We investigate the physical mechanisms responsible for the observed spectral lines using appropriate diagnostic diagrams and ionization models. We find that the H II regions are being photoionized by star clusters with ages ~ 2.5 –20 Myr and ionization potential $-3.5 < \log \langle U \rangle < -3.0$. In these diagrams, a binary population is needed to reproduce the observables considered in this work.

Key words: stars: Wolf–Rayet – H II regions – galaxies: abundances – galaxies: individual: AM 0644-741.

1 INTRODUCTION

Ring galaxies are a class of peculiar galaxies (Arp 1966) that have apparent ring-like morphologies in optical images (Arp & Madore 1987). Nowadays, ring galaxies are understood as the outcome of a rare-type (1 in 1000) of a head-on collisional event: a satellite compact galaxy crashes through another’s primary disc, and the resulting ring is the conspicuous short-lived evidence of this collision ($t_{\text{dyn}} \sim 10^8$ yr; Madore, Nelson & Petrillo 2009). Ring galaxies thus are an excellent laboratory to study the evolution of galaxies, particularly the triggering and suppression of star formation on galactic scales after such interactions (Higdon, Higdon & Rand 2011). In the most recent atlas of collisional ring galaxies, Madore, Nelson & Petrillo (2009) report 127 ring galaxies known so far in the local Universe, of which 108 are located in the Southern hemisphere and 19 have positive declinations. However, the search for ring galaxies is far from complete and we could expect at least

a similar number in the Northern hemisphere. Projects like DESI Legacy Imaging Surveys (Dey et al. 2019) could help with this purpose in the near future.

In order to analyse the star formation triggered in the rings of these systems we started a series of studies of ring-type galaxies with available integral field spectroscopy (IFS) observations. In Zaragoza-Cardiel et al. (2022) and Mayya et al. (2023) we focused on Cartwheel, the archetypal ring galaxy and the most observed and modelled galaxy of its category (e.g. Higdon 1995; Renaud et al. 2018). However, there is an even rarer and short lived collisional byproduct subclass: the ‘double-ringed’ galaxies, which has also been predicted in numerical simulations by Lynds & Toomre (1976). Here, we study the double-ringed galaxy AM 0644-741, a.k.a the Lindsay–Shapley (L–S) ring, located at a distance of 98.6 Mpc, assuming a Hubble constant $H_0 = 67.8 \text{ km s}^{-1} \text{ Mpc}^{-1}$, $\Omega_m = 0.308$, $\Omega_\Lambda = 0.692$ (NASA NED¹).

¹The NASA/IPAC Extragalactic Database (NED) is funded by the National Aeronautics and Space Administration and operated by the California Institute of Technology.

* E-mail: mau.gglez@gmail.com

AM0644-741 is characterized by its striking double-ring of H II regions and star cluster complexes noticeable in optical bands, particularly in H α (see Fig. 1), but also in the near and far-UV, tracing recent bursts of star formation. The ring, presumably driven by a radially expanding density wave triggered by the collision of a satellite object nearly perpendicular to the plane of its disc and close to its centre (Lynds & Toomre 1976; Higdon, Higdon & Rand 2011), has an angular diameter of 97 arcsec, the second largest (after AM 1724-622 with 125 arcsec) reported in the Southern Catalogue of ring galaxies by Madore, Nelson & Petrillo (2009), corresponding to a physical size of ~ 46.4 kpc, using the mentioned distance. A slightly lower value for the major axis is reported by Higdon, Higdon & Rand (2011, see Table 1), but differences are minor. The nucleus is north of the geometric center of the elliptical ring, in the direction of the major axis. Compared to the ring, the inner disc is distinctively more red and gas depleted, with a presumed older stellar population, given the absence of H II regions ionized by young stars. Unlike its ‘cousin’ the Cartwheel, AM0644-741 does not show a network of spokes in its inner disc, which is practically transparent in the referred bands. Few, Madore & Arp (1982) reported that the double-ring is rotating at 311 ± 19 km s $^{-1}$ and is expanding at a velocity (V_{exp}) of 128 ± 12 km s $^{-1}$, giving a dynamical age ($R_{\text{ring}}/V_{\text{exp}}$) ~ 175 Myr. In Table 1, we list the main physical parameters of AM0644-741 collected from literature.

According to the Madore, Nelson & Petrillo (2009) atlas, every ring galaxy has a likely collider detected in optical bands. AM0644-741 is not an exception, having at least three identified candidates: C1, C2, and C3, with a projected separation from the ring nucleus of 78, 110, and 326 arcsec, respectively, and heliocentric velocities of 7000, 6750, and 6430 km s $^{-1}$, respectively (see table 1 and fig. 5 in Madore, Nelson & Petrillo 2009). Assuming roughly the same distance as the L–S ring, this is equivalent to a separation between the galaxies of 37, 53, and 156 kpc, respectively. So far, the true collider has not yet been identified and this issue remains unresolved.

Higdon & Wallin (1997) were the first to report the massive star formation distribution and the basic properties of 54 star-forming regions in this galaxy; we indicate these regions in Fig. 1 (orange dashed circles) as a reference. Later, Higdon, Higdon & Rand (2011) studied the impact of star formation on the neutral interstellar medium (ISM). Since then, no comprehensive study has been carried out on this galaxy. The availability of spectrographs incorporating integral field units (IFUs) on large telescopes such as Multi Unit Spectroscopic Explorer (MUSE) on the Very Large Telescope (VLT; Bacon et al. 2010) allows a new in-depth study of AM0644-741. One MUSE data set is available on this galaxy at the seeing-limited spatial resolution of 1.161 arcsec. This data set provides optical spectra covering a range of 4750–9350 Å (corresponding to a rest wavelength range of 4650–9250 Å, considering its redshift: $z = 0.022$) over the entire galaxy.

MUSE datacubes of ring galaxies offers the opportunity to address several problems that are particular to the ring galaxies. The first of those is the study of metallic abundances and its radial gradient. Also, ring galaxies are known to be prolific sources of Ultra Luminous X-ray (ULX) sources (Wolter, Fruscione & Mapelli 2018). MUSE data offers an opportunity to study the impact of these sources on the state of high ionization potential emission lines from [Ar IV] and He II. X-ray sources are often postulated to be responsible of these ions (Schaefer, Fragos & Izotov 2019). Furthermore, star-forming regions pass through the WR phase for a short term during which time the blue part of the spectrum is expected to contain the so-called ‘blue-bump’ (hereafter, BB), made up basically of broad emission lines such as He II and, depending on the WR-type, with contributions

of C III–C IV or N III–N V. However, the detection of BB is heavily metallicity dependent. All these phenomena have been addressed in the Cartwheel using the MUSE data in our previous papers (Zaragoza-Cardiel et al. 2022; Mayya et al. 2023). For example, in the Cartwheel, which has around $1/4 Z_{\odot}$, we found enrichment of O in the ring H II regions without the corresponding enrichment in N and Fe, metals expelled by intermediate-age and low-mass stars. In the Cartwheel, we did not find signature of X-ray ionization even in H II regions coinciding with ULXs, and those where He II $\lambda 4686$ line is detected.

We employ the available MUSE observations to continue our series of studies on the star formation triggered in the ring of this type of galaxies. Here in particular, we study the ionizing mechanisms and the chemical abundances in the star cluster complexes hosted in the H II regions that shape the double-ringed morphology of AM0644-741. We are interested in comparing our results in this galaxy with those obtained in the Cartwheel, to better understand the nature and evolution of ring structures in galaxies with different environments, star formation histories and metallicities in its post-collisional stage. Thanks to new spectroscopic data cubes like those of MUSE/VLT these studies are now possible. In a H α image we constructed using the MUSE data set (see Section 2) we identified 179 H II regions in the double-ring of AM0644-741. At the distance of the L–S ring, MUSE spectra are available at physical scales of ~ 556 pc. At the spatial resolution of the Advanced Camera for Surveys (ACS) Wide Field Channel (WFC) images of the Hubble Space Telescope (HST), which are the highest resolution images available for AM0644-741 (0.05 arcsec per pix), we can associate each MUSE-identified H II region with a population of super star clusters, which presumably provide the ionization of the H II regions. A colour-composite image using our MUSE H α image and HST filters is shown in Fig. 1. All images used in this figure are astrometrized as explained in Section 2.2. However, the point spread function (PSF) of the images are not matched and correspond to the respective observed values given in the section below.

This article is structured as follows: in Section 2, we describe the spectroscopic data set, the constructed catalogue of H II regions, the extraction of the spectra and measurement of the emission line fluxes; in Section 3, we determine the abundances of our objects; we study the ionization sources with diagnostic diagrams and models in Section 4; our results are discussed in Section 5; finally, a summary and our conclusions are given in Section 6.

2 SPECTROSCOPIC DATA

2.1 VLT/MUSE observations

MUSE is a panoramic integral-field spectrograph at the 8-m VLT of the European Southern Observatory (ESO),² operating in the optical wavelength range from ~ 4750 to ~ 9351 Å with a spatial sampling of 0.2 arcsec pixel $^{-1}$, a spectral sampling of 1.25 Å pixel $^{-1}$ and a spectral resolution FWHM ~ 3 Å (Bacon et al. 2010). This spectral resolution corresponds to $\sigma \sim 40$ –60 km s $^{-1}$, which is not good enough to resolve the lines but sufficient to detect the strong lines to measure abundances. The public MUSE data cube of AM0644-741 galaxy was retrieved from the ESO Science Archive Facility.³ The data cube was already flux and wavelength calibrated, ready for scientific exploitation. The data were obtained during a single

²<http://muse-vlt.eu/science/>

³<http://archive.eso.org/cms.html>

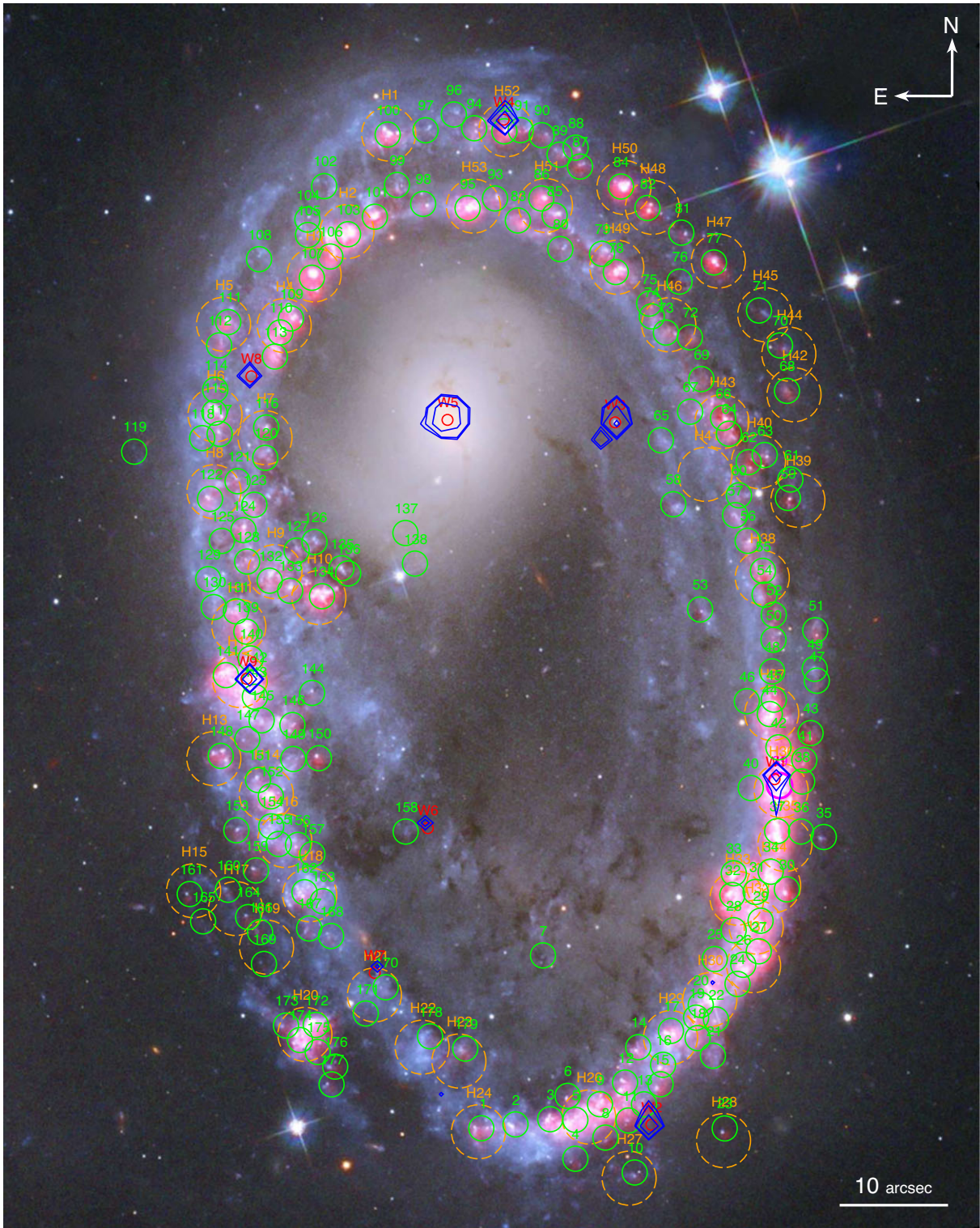


Figure 1. Colour-composite image of the double-ring galaxy AM 0644-741, formed using the HST/ACS/WFC images in the filters $F814W$, $F625W$, and $F435W$ as red, green, and blue components, respectively; and a new $H\alpha$ image constructed from MUSE data (FWHM = 1.161 arcsec) as a fourth reddish component. The 179 H II regions studied here are identified by green circles of 1.162 arcsec radius (~ 556 pc at $D = 98.62$ Mpc), which is twice the sky resolution size of MUSE. Star-forming regions from Higdon & Wallin (1997) are indicated in dashed orange circles (H1–H53), and the location of X-ray sources, some of them ULXs, from Wolter, Fruscione & Mapelli (2018) by red circles (W1–W9) and their positional error ellipses with blue contours. The majority of H II regions identified with MUSE are associated with a star formation complex resolved by HST. Although ULX sources are located in the star-forming ring, its association with a cluster is not straightforward. The brightest H II region, ID 39, is also a WR cluster coinciding with the location of the most luminous ULX (W1). See text for details.

Table 1. Parameters of the double-ringed galaxy AM 0644-741.

Parameter	Value	Ref.
Cross-identifications	ESO 034-IG 011	(a)
	IRAS 06443-7411	(a)
Galaxy type	Lindsay–Shapley ring	(a)
Right ascension (J2000)	06h43m06.1s	(a)
Declination (J2000)	−74d13m35s	(a)
z (Helio)	0.02203 ± 0.00009	(b)
Velocity (Heliocentric) [km s ^{−1}]	6604 ± 26	(b)
Hubble distance (CMB) [Mpc]	98.62 ± 6.91	(a)
Foreground Gal. ext. (A_V) [mag]	0.3537	(c)
Z [Z_\odot] (Bulge spectra)	0.45	(d)
Angular diameter [arcsec]	95×52	(e)
Physical diam. [kpc]	45×25	
$L_{\text{H}\alpha}$ [10 ⁴² erg s ^{−1}]	1.40 ± 0.06	(e)
L_X (0.5–10 keV) [10 ⁴¹ erg s ^{−1}]	1.78	(g)
$\text{EW}_{\text{H}\alpha}$ [Å]	14	(f)
SFR [M_\odot yr ^{−1}] (from L(H α))	11.2 ± 0.4	(e)
SFR [M_\odot yr ^{−1}] (from radio)	17.6 ± 0.9	(g)
V_{rot} [km s ^{−1}]	311 ± 19	(h)
V_{exp} [km s ^{−1}]	128 ± 12	(h)

Note. (a) NASA NED; (b) Fisher et al. (1995); (c) Schlafly & Finkbeiner (2011); (d) Mapelli, Colpi & Zampieri (2009, and references therein); (e) Higdon, Higdon & Rand (2011); (f) Higdon & Wallin (1997, and references therein); (g) Wolter, Fruscione & Mapelli (2018); (h) Few, Madore & Arp (1982).

observing run on November 9, 2020; the Principal Investigator (PI) is Bernd Husemann (Program ID: 106.2155); dedicating a total exposure time of =1350 s (effective time of =714.5 s) in a single observation. A sky coverage of observations of 2.1 arcmin², encloses the entire star-forming ring of the AM 0644-741 galaxy, as can be seen in Fig. 1; here we show an RGB image formed by combining the HST/ACS/WFC filters in F814W, F625W and F435W as red, green and blue components, respectively; the H α image constructed from MUSE data is used as a fourth reddish component. The MUSE images have a seeing-limited resolution of Full Width at Half Maximum (FWHM) of 1.162 arcsec, which corresponds to a spatial scale of ~ 556 pc at the distance of the L-S ring galaxy. We list the main observation details in Table 2.

2.2 MUSE data cube and astrometry

We used the reduced 3-D data cube as a starting point in our analysis. The tool QFitsView⁴ (Ott 2012) was used for the extraction of images at selected wavelengths, as well as spectra of selected regions. A continuum image covering the entire spectral range of MUSE is prepared to transform MUSE images into International Celestial Reference System (ICRS) as defined by the coordinates of the point sources in the 2MASS catalogue. The Field of View (FoV) of the MUSE image of AM 0644-741 contains three 2MASS stars which is insufficient to obtain accurate solutions. We hence carried out the astrometry in two steps, first we brought the HST F814W images into ICRS using 14 2MASS stars, and then we identified 13 compact objects in the MUSE continuum image and the F814W image, which we used to find astrometric solution of the MUSE image. The astrometric accuracy of the resulting image is 0.1 arcsec. We used the IRAF tasks *ccmap* and *wregister* to carry out the astrometric calibration.

⁴<https://www.mpe.mpg.de/~ott/dpuser/qfitsview.html>

Table 2. Details of the VLT-MUSE data set[†] of AM 0644-741.

Parameter	
R.A. (J2000)	06:43:05.01
Dec. (J2000)	−74:14:28.4
Date of observation	09/11/2020
Sky coverage	2.1 arcmin ²
Sky resolution ^{††}	1.162 arcsec
Pixel scale	0.2 arcsec
Spectral range	4750–9350 Å
Spectral resolution (R)	3027
Effective exposure time	714.5 s
Sensitivity (AB mag at 5 σ)	20.87 mag

Notes. [†] Single IFU cube; data processing certified by ESO; PI: B. Husemann; OB ID: 2885683.

^{††} FWHM effective spatial resolution.

2.3 Catalog

For our study in AM 0644-741 it was necessary to build a new catalog of H II regions using the available MUSE observations. As a first step, we generated a continuum-free H α image from the MUSE datacube using QFitsView. For achieving this, we summed fluxes in a 8.8 Å window centered on H α at the redshifted wavelength of this galaxy subtracting a continuum 44 Å away on either side of the H α line. With these values we ensure that the emission line is covered by the width of the filter, taking into account the shift of the lines due to its kinematics.

The continuum-subtracted H α image (the reddish component in Fig. 1) allows the identification of H II regions using source extractor codes such as PYHIIEXTRACTOR (Lugo-Aranda et al. 2022), SExtractor (Bertin & Arnouts 1996), etc. The former code measures accurate fluxes of H II regions, taking into account corrugated boundaries. We opted to measure fluxes by fitting a Gaussian function to line profiles on spectra extracted using circular apertures of fixed radius around the identified regions. This method ensures that the fluxes of all lines are measured over the same areas. For this reason, we used SExtractor to identify the locations of the objects for later extraction of their spectra. We identified a total of 184 regions with H α emission in the entire FoV of this galaxy. Then, spectra were extracted with apertures of 1.162 arcsec radius, which is equivalent to 1 seeing FWHM, for all regions automatically selected. Finally, after careful inspection of the spectra, five objects were later identified to be spurious sources (which include the nucleus of the galaxy and probable background stars), ultimately resulting in a catalog of 179 H II regions. Most of these sources are located in the double-ring of the galaxy (see Fig. 1). The spectrum of the most conspicuous H II region in AM 0644-741 is shown in Fig. 2. The foreground Galactic extinction in the direction of AM 0644-741 is $A_V = 0.35$ mag (Schlafly & Finkbeiner 2011). The extracted spectra were first corrected for this foreground extinction using the Galactic reddening curve of Cardelli, Clayton & Mathis (1989). The selected regions are at least an order of magnitude brighter in surface brightness with respect to the diffuse ionized gas (DIG), implying that the contamination of the observed line ratios by the DIG is negligible. Moreover with the recent understanding that the DIG in star-forming galaxies is created due to photoionization by the photons leaking the H II regions (Della Bruna et al. 2020; Belfiore et al. 2022), it is expected to occupy the immediate surroundings of H II regions in the disk rather than the regions along the line of sight to H II regions. Hence, we did not apply any correction to the observed line ratios.

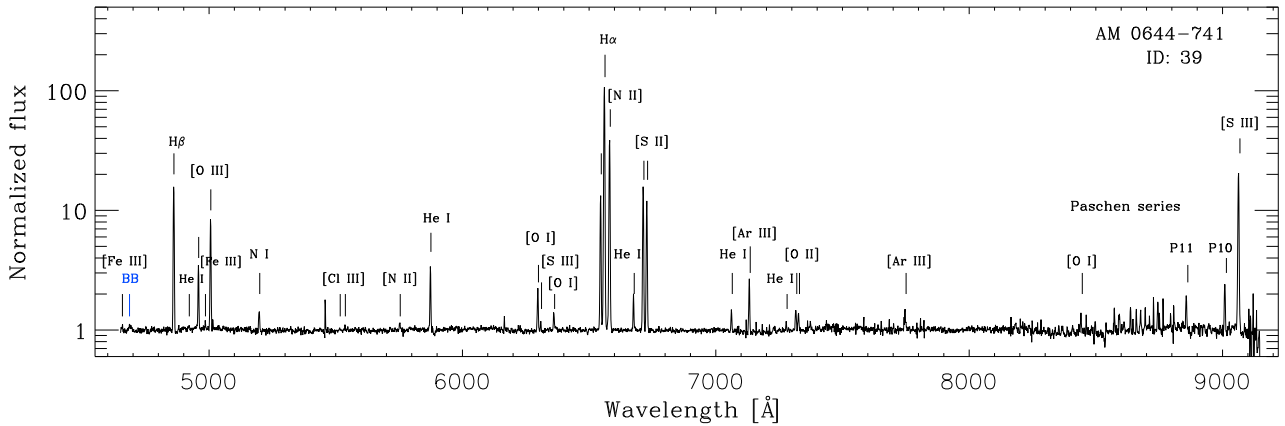


Figure 2. VLT MUSE redshift-corrected spectrum of the cluster complex ID 39, WR1, located in the SW section of the ring of the AM 0644-741 galaxy (see Fig. 1). The so-called ‘blue-bump’ (BB) WR feature at 4686 Å, as well as the most common nebular lines of typical H II regions, from [Fe III] at 4658 Å to [S III] at 9068.6 Å, are indicated. The spectrum is shown normalized to its best-fitting continuum.

AM 0644-741 has nine identified X-ray sources of which, excluding the galaxy nucleus and a background active galactic nucleus (AGN), seven were identified as ULXs by Wolter, Fruscione & Mapelli (2018). The ULX sources are located in the ring of the galaxy and some of them coincide with the projected location of an H II region hosting a star-forming complex (see Fig. 1). At least three of the ULXs in the ring are associated with a H II region of our sample. We address the nature and probable role of the ULXs in the ionization of their host H II regions in Section 4.

2.4 Measurement of line fluxes

The analysis of the ionizing mechanisms of the H II regions in the double-ring of AM 0644-741 and the determination of their nebular abundances requires the previous determination of de-reddened flux ratios of the nebular lines relative to the flux of H β. Considering that our sample of H II regions might be affected by the presence of an underlying absorption feature (e.g. Balmer lines, H β in particular), first we fitted their continuum with Single Stellar Population (SSP) synthesis models. We used the GIST pipeline (Bittner et al. 2019), making use of the most recent Charlot & Bruzual SSP models (Charlot & Bruzual, in preparation), to fit the continuum and the absorption lines over the entire observed wavelength range of our spectra: 4650–9250 Å, where the MUSE spectral resolution is ~3 Å. Then we subtracted the fitted continuum to obtain pure nebular spectra, which is the one we used for later analysis.

Around 30 nebular lines were identified, from [Fe III] at 4658 Å to [S III] at 9068.6 Å, in the spectrum of the brightest H II region in AM 0644-741, ID 39, most of which have been marked in Fig. 2. These lines were analysed using the Gaussian line fitting option of the IRAF task *splot*. The measured line fluxes were corrected for extinction by using the obtained $c(H\beta)$ value assuming an intrinsic Balmer-decrement ratio of $H\alpha/H\beta = 2.86$, for a case B photoionised nebula, corresponding to mean values for T_e in the range 2000 K and 12000 K and n_e between 100 cm^{-3} and 1200 cm^{-3} (see Osterbrock & Ferland 2006). We used the reddening curve of Cardelli, Clayton & Mathis (1989) with $R_V = 3.1$. The resultant line fluxes and statistical errors are listed in Table 3 for the brightest H II region of the sample.

The spectrum of ID 39 shows a Wolf-Rayet (WR) feature, the BB, at 4686 Å (Allen, Wright & Goss 1976; Kunth & Sargent 1981). This feature has been observed both in metal-rich (e.g. the Antennae galaxies by Gómez-González et al. 2021, at 18.1 Mpc), LMC-like

Table 3. De-reddened nebular line fluxes relative to $H\beta = 100$ for the H II region ID 39 in AM 0644-741 (see Fig. 1). Its spectrum is shown in Fig. 2. The complete information for all the H II regions is given as extra material.

λ_0 (Å)	Ion	Flux (2.3 arcsec)
4658.0	[Fe III]	0.55 ± 0.17
4711.4	[Ar IV]	0.48 ± 0.15
4740.2	[Ar IV]	0.47 ± 0.15
4861.4	H β	100
4921.9	He I	0.38 ± 0.13
4958.9	[O III]	14.87 ± 0.16
4985.9	[Fe III]	1.02 ± 0.18
5006.8	[O III]	43.71 ± 0.04
5200.0	N I	2.92 ± 0.21
5517.7	[Cl III]	0.20 ± 0.08
5754.6	[N II]	0.72 ± 0.17
5875.6	He I	8.58 ± 0.22
6300.0	[O I]	3.82 ± 0.15
6312.1	[S III]	0.45 ± 0.14
6363.8	[O I]	1.31 ± 0.15
6548.1	[N II]	33.35 ± 0.04
6562.8	H α	287 ± 2.25
6583.5	[N II]	101.91 ± 0.69
6678.2	He I	2.34 ± 0.13
6716.4	[S II]	38.41 ± 0.07
6730.8	[S II]	28.10 ± 0.05
7065.2	He I	1.07 ± 0.19
7135.8	[Ar III]	3.75 ± 0.13
7170.5	[Ar III]	0.16 ± 0.09
7281.3	He I	0.32 ± 0.09
7319.2	[O II]	1.26 ± 0.15
7330.2	[O II]	0.97 ± 0.16
7751.1	[Ar III]	1.17 ± 0.17
8446.4	[O I]	0.42 ± 0.22
8665.0	P 13	0.46 ± 0.17
8750.5	P 12	1.02 ± 0.18
8862.9	P 11	1.22 ± 0.22
9015.3	P 10	1.59 ± 0.19
9068.6	[S III]	19.57 ± 0.36
$\log(F(H\beta))$		$-13.567 \pm 0.007\text{ erg cm}^{-2}\text{ s}^{-1}$
A_V		$1.225 \pm 0.014\text{ mag}$
$c(H\beta)$		$0.730 \pm 0.007\text{ mag}$
$EW(H\beta)$		55.75 Å
$SNR(H\beta)$		141.2

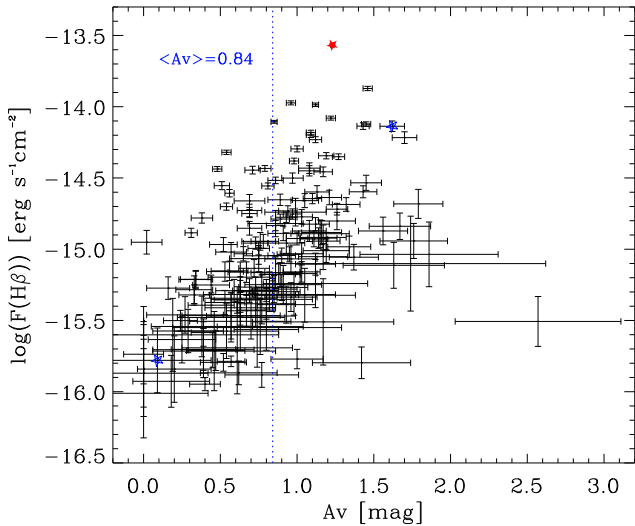


Figure 3. Distribution of the visual extinction A_V and the reddening corrected $F(H\beta)$ of the H II regions in the double-ring of AM0644-741. The average value of $A_V = 0.84$ mag is shown by the vertical dashed line. A_V tends to increase with $F(H\beta)$. The star symbols indicates the H II regions with a ULX counterpart (ID 39, 92, and 142). The red star represents the H II region (ID 39) with a WR feature in its spectrum.

(e.g. NGC 3125 by Hadfield & Crowther 2006, at 11.5 Mpc) and metal-poor galaxies (e.g. Mrk 178, NGC 625 by Kehrig et al. 2013; Monreal-Ibero et al. 2017, at 3.9 Mpc). Recent BB detections also include M 81 (Gómez-González, Mayya & Rosa-González 2016, at 3.6 Mpc) We address the nature of the BB in ID 39 (hereafter WR1) in Section 4.1.

Reddening-corrected fluxes for all the objects are reported in a Table as extra-material. The distribution of the visual extinction (A_V) and the reddening corrected $F(H\beta)$ is shown in Fig. 3. It can be noticed that A_V tends to increase with $F(H\beta)$. A median value of $A_V \sim 0.84$ mag is indicated by a dotted vertical line. The correlation between A_V and $F(H\beta)$ arises because the analyzed H II regions adhere to a Kennicutt-Schmidt star-formation relation (Barrera-Ballesteros et al. 2020). In other words, the gas density of a star-forming region, which dictates A_V through the almost constant gas-to-dust ratio, correlates with the star formation rate (SFR), which is traced by $H\beta$. It can be recalled that Cartwheel H II regions do not show such a correlation (Zaragoza-Cardiel et al. 2022). The median values obtained here are lower than the corresponding values for the bright ring H II regions in the Cartwheel but are comparable to the median A_V of the fainter regions in the outer ring of the Cartwheel.

3 DETERMINATION OF CHEMICAL ABUNDANCES

3.1 Direct method

Temperature-sensitive lines are detected in only one (ID 39,) of the 179 H II regions in AM0644-741, making it possible to determine abundance using the direct method (DM) only for this region. This happens to be the brightest nebular region with $\log(F(H\beta)/[\text{erg cm}^{-2} \text{s}^{-1}]) = -13.567 \pm 0.007$ (see Fig. 3) and $\text{SNR}(H\beta)=141$ (see Table A1) and host the only regions where a WR feature is detected (see Fig. 2) the location of this brightest H II region also coincides with the brightest ULX (W1) reported in this galaxy (see Fig. 1). Determining the O abundance of this region is key

Table 4. T_e , n_e and He, O, N and Fe ionic abundances using the DM for ID 39 (WR1) in AM0644-741.

Parameter	Note	Value
$T_e^{\text{low}}[\text{N II}]$		7726 ± 488 K
$T_e^{\text{medium}}[\text{S III}]$		6853 ± 641 K
T_e^{high}	Relation from Garnett (1992)	8448 ± 772 K
n_e	$T_e^{\text{low}}[\text{N II}]$	54 ± 2 cm $^{-3}$
n_e	$T_e^{\text{medium}}[\text{S III}]$	53 ± 2 cm $^{-3}$
$12 + \log(\frac{\text{He}}{\text{H}})$	He $^+$ component	10.75 ± 0.14
$\log(\frac{\text{N}}{\text{O}})$		-1.3 ± 0.2
$12 + \log(\frac{\text{O}}{\text{H}})$		8.9 ± 0.2
$\log(\frac{\text{Fe}}{\text{O}})$		-2.7 ± 0.3

to estimate the WR population responsible for the broad He II $\lambda 4686$ line. We address this issue in Section 4.1.

We followed the methodology used to determine O abundances in the Cartwheel H II regions (Zaragoza-Cardiel et al. 2022). First, we determined the physical conditions of the ionized gas: electron temperature (T_e) and electron density (n_e). T_e and n_e are estimated simultaneously with PyNeb (Luridiana, Morisset & Shaw 2015). We use the three ionization zones approximation from Garnett (1992): T_e for the low ionization zone (T_e^{low}) was determined with $[\text{N II}](\lambda 6548 + \lambda 6584)/\lambda 5755$; the medium ionization zone (T_e^{medium}) with $[\text{S III}]\lambda 6312/\lambda 9069$ and the high ionization zone ($T_e^{\text{high}} = T_e^{[\text{O III}]}$) using its relation with T_e^{medium} from Hägele et al. (2006):

$$T_e^{\text{medium}} = 1.19 T_e^{\text{high}} - 3200\text{K}. \quad (1)$$

Densities determined from $[\text{S II}]\lambda 6717/\lambda 6731$ were used for all the three zone lines. In Table 4, we list our results for T_e , n_e , the ionic abundances of He, N, O, and Fe for WR1.

In Fig. 4, we compare $\log(\frac{\text{N}}{\text{O}})$ versus $12 + \log(\frac{\text{O}}{\text{H}})$ for the WR H II region detected in AM0644-741 with H II regions in other galaxies: the prototype ring-galaxy Cartwheel (Zaragoza-Cardiel et al. 2022) and other ring galaxies (Bransford et al. 1998); with irregular galaxies (Garnett 1990); and other well known galaxies like M 101 (Kennicutt, Bresolin & Garnett 2003), M 31 (Zurita & Bresolin 2012), M 33 (Toribio San Cipriano et al. 2016), and M 81 (Magrini, Gonçalves & Vajgel 2017), with H II regions of a sample of galaxies studied by Arellano-Córdova & Rodríguez (2020) and objects from the CALIFA survey (Espinosa-Ponce et al. 2020). Note that all abundances, except those from Bransford et al. (1998) and Espinosa-Ponce et al. (2020), are obtained using the DM. Following Zaragoza-Cardiel et al. (2022), we also indicate the schematic representation of the expected evolution of the N/O ratio for a dwarf galaxy from Garnett (1990) as a reference. The N/O ratio of WR1 is close to H II regions in other irregular galaxies. However, the O abundance for AM0644-741, with $12 + \log(\frac{\text{O}}{\text{H}}) = 8.9$, is higher by as much as 0.6 dex, and is among the highest values measured using the DM. It is likely that the equation that we have used to determine temperature of the high ionization zone, obtained for low metallicity irregular galaxies, underestimates the temperature, thus slightly overestimating the abundances. Temperature calibrations for high metallicity regions are lacking (see e.g. Arellano-Córdova & Rodríguez 2020).

In Fig. 5, we compare $\log(\frac{\text{Fe}}{\text{O}})$ versus $12 + \log(\frac{\text{O}}{\text{H}})$ for WR1 with the H II regions in Cartwheel (Zaragoza-Cardiel et al. 2022), in the Milky Way (MW; Rodríguez 2002; Delgado-Inglada et al. 2016) and in M33 (Toribio San Cipriano et al. 2016). WR1 in AM0644-741 follows the trend of the H II regions in these galaxies, the higher the abundance of O, the lower that of Fe. However, the measured O

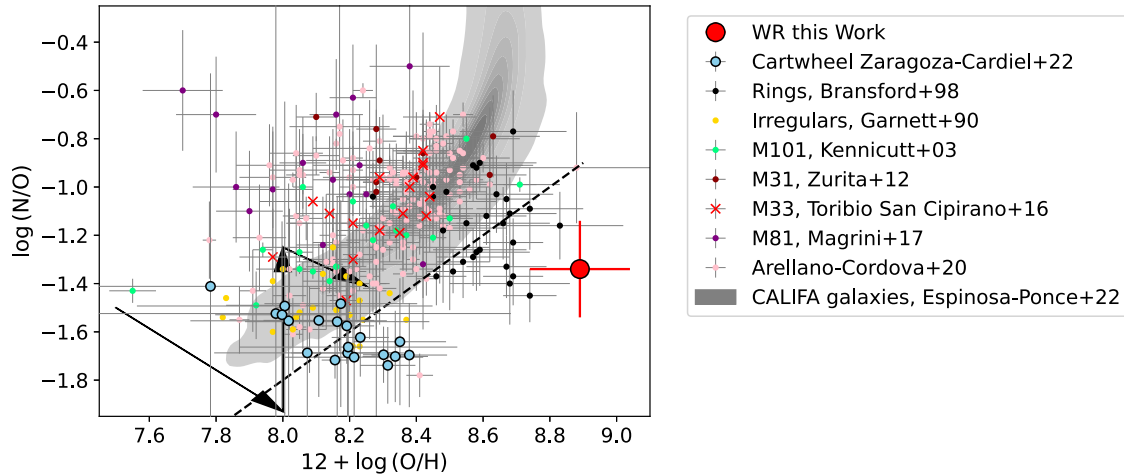


Figure 4. $\log(\frac{N}{O})$ versus $12 + \log(\frac{O}{H})$ for the WR H II region (red circle) detected in AM0644-741. N and O abundances were determined with the DM. Following Zaragoza-Cardiel et al. (2022), we compare our results with the corresponding values reported for H II regions in other systems: Cartwheel (Zaragoza-Cardiel et al. 2022, blue dots); ring galaxies (Bransford et al. 1998, black dots); irregular galaxies (Garnett 1990, yellow dots); M101 (Kennicutt, Bresolin & Garnett 2003, green dots); M31 (Zurita & Bresolin 2012, red dots); M33 (Toribio San Cipriano et al. 2016, red crosses) and M81 (Magrini, Gonçalves & Vajgel 2017, purple dots); H II regions of several galaxies studied by Arellano-Córdova & Rodríguez (2020, pink dots) and results from the CALIFA survey (Espinosa-Ponce et al. 2020, grey region). Following Zaragoza-Cardiel et al. (2022) we indicate the schematic representation of the evolution of the N/O ratio for a dwarf galaxy from Garnett (1990).

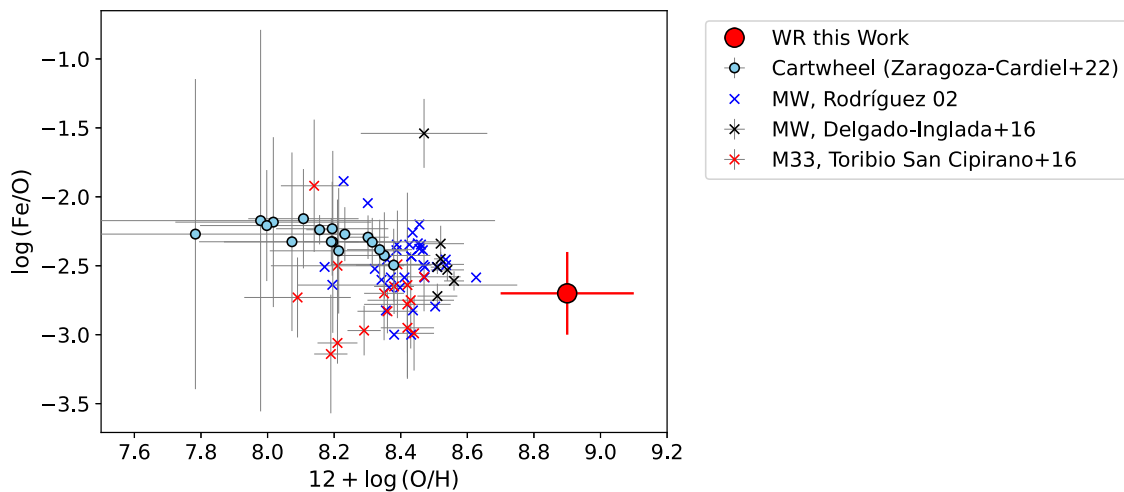


Figure 5. $\log(\frac{Fe}{O})$ versus $12 + \log(\frac{O}{H})$ for the WR H II region (red circle) detected in AM0644-741. Fe and O abundances were determined with the DM. Following Zaragoza-Cardiel et al. (2022), we compare our results with the corresponding values reported for H II regions in other systems: Cartwheel (Zaragoza-Cardiel et al. 2022, blue dots); the Milky Way by Rodríguez (2002, blue crosses) and Delgado-Inglada et al. (2016, red crosses) and in M33 (Toribio San Cipriano et al. 2016, red crosses).

abundance in AM0644-741 is a clear outlier, which as mentioned above, is likely due to the lack of reliable metallicity calibrations at the high-metallicity end.

3.2 Strong-line method

We determined the abundances using the strong-line method (SLM) for all the H II regions in which we could detect [O III], [N II], and [S II] lines at SNR > 3. As we did in the Cartwheel galaxy (see Zaragoza-Cardiel et al. 2022), we used the empirical ‘S-calibrator’ from Pilyugin & Grebel (2016), since the strong lines used are all in the MUSE spectral range: H β , H α , [O III] λ 4959 + λ 5007, [N II] λ 6548 + λ 6584, and [S II] λ 6717 + λ 6731. Abundances could be determined for 137 regions of the sample.

In order to check for any gradient, galactocentric or azimuthal, of the O abundances in the double-ring of AM0644-741, we used a set of ellipses indicated in Fig. 6 to define a galactocentric radius (R) and position angle (PA) of our catalogue of H II regions. AM0644-741 resembles its cousin Cartwheel in the sense that the nucleus is not at the geometrical centre of the star-forming elliptical ring. We hence followed the moving-centre method adopted by Marcum, Appleton & Higdon (1992) for the Cartwheel to define the ellipses. In this method, the centre of successive ellipses is changed smoothly from the nucleus for the inner ellipses to the centre of the ring of the outer ellipses. A more detailed description of this procedure is given in Zaragoza-Cardiel et al. (2022, in their section 4.3).

In Fig. 7, we plot the O abundance of the H II regions versus the galactocentric radius. We indicate the median value

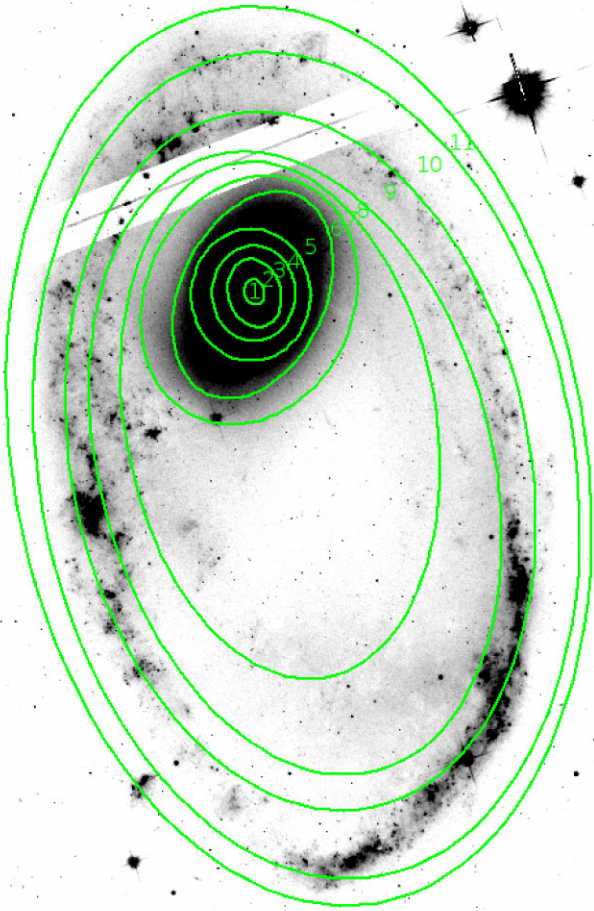


Figure 6. HST/ACS/WFC image in $F625W$ filter of AM0644-741 with the ellipses (1 – 11) used to estimate the galactocentric radius and position angle of the H II regions in the star-forming double-ring of this galaxy.

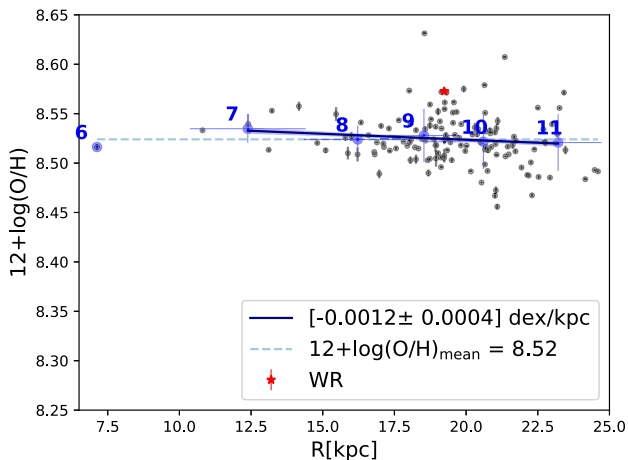


Figure 7. $12 + \log(\frac{O}{H})$ versus galactocentric radius (R) for the H II regions (black points) located in the double ring of AM0644-741. Average values for the regions amidst the ellipses defined in Fig. 6 are indicated with blue points. O abundances were determined with the SLM; the blue dashed line indicates the median value. A linear fit (blue line) to the L–S ring data points indicates a slight gradient of -0.0012 ± 0.0004 dex kpc^{-1} among the ellipses 7 and 11. The red star represents the H II region (ID 39) with the WR feature.

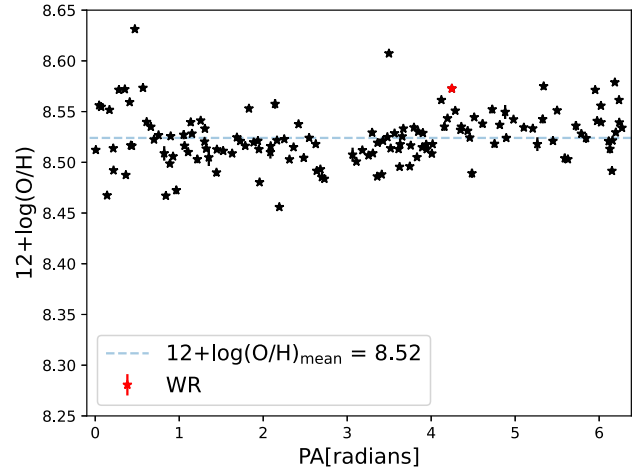


Figure 8. $12 + \log(\frac{O}{H})$ versus PA for the H II regions (black stars) in the double ring of AM0644-741. O abundances were determined with the SLM. The median value is indicated with a blue dashed line. There is no indication of an azimuthal gradient. The WR region is indicated by a red star.

of $12 + \log(\frac{O}{H}) = 8.52$. By a linear fit to the L–S ring data points, we get a slight slope indicating a small gradient of -0.0012 ± 0.0004 dex kpc^{-1} . In comparison, the Cartwheel shows a gradient of -0.017 ± 0.0001 dex kpc^{-1} (Zaragoza-Cardiel et al. 2022) which is comparable to values found in spiral galaxies (Sánchez 2020). We find the SLM-determined O abundance of WR1 is slightly above the median value, but only by 0.05 dex. In Fig. 8, we show the O abundances versus its position angle (PA). Here, we did not find any indication of an azimuthal gradient. We list our results for each object in Table A1. It may be noted that the O abundance of WR1 determined from the DM is ~ 0.3 dex higher than that determined from the SLM, which is marginally higher than the 0.2 dex error in the former method.

4 IONIZATION STATE OF THE H II REGIONS

The availability of spectra covering almost the entire optical range allow us to address the ionization mechanisms of the $H\alpha$ -emitting regions in the MUSE FoV. We use Xiao, Stanway & Eldridge (2018) calculations based on BPASS (Eldridge et al. 2017) and CLOUDY (Ferland et al. 1998) models in standard BPT diagrams (Baldwin, Phillips & Terlevich 1981) to study the ionization sources in the double ring of AM0644-741. We also discuss the role of the WRs and ULXs in the ionization when H II regions are associated with these sources.

4.1 H II region containing WR stars

WR stars are formally defined by their emission-line dominated spectra arising from their strong winds. The core-He burning objects among them, also called ‘classical’ WR stars, represent a late stage in the evolution of massive stars, where a considerable amount of their outer layer has been lost. Assuming single-star evolution, WR stars start their lives on the main sequence as O stars with $M_{\text{init}} \geq 25 M_{\odot}$ at Z_{\odot} (e.g. Georgy et al. 2012; Chieffi & Limongi 2013; Chen et al. 2015). See also Massey (2003) for estimated masses ($M_{\text{init}} \geq 20 M_{\odot}$) of the progenitor stars for different WR types, at different metallicities. While different assumptions about mass-loss or the formation of a WR stars due to binary interaction can

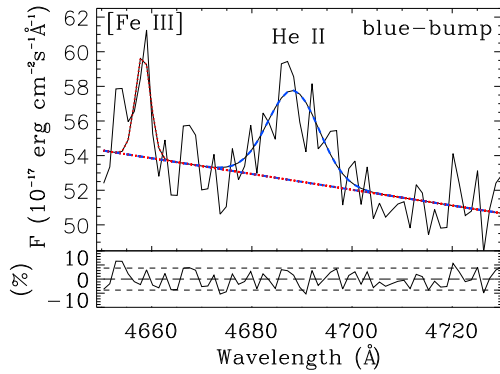


Figure 9. Gaussian fit to the BB of the H II region ID 39, WR1. The blue dashed line represents the fit to the broad WR feature, He II $\lambda 4686$, and the red dotted line the fit to the narrow nebular line. The sum is shown in black. The fitted continuum is shown by the dashed straight line. The residuals are shown at the bottom of the panel (in per cent). The results are listed in Table 5.

shift the absolute mass limits, all WR stars are so massive that they usually cannot be much older than $\sim 2\text{--}4$ Myr when reaching the (classical) WR stage. Characterized by significant mass-loss rates of $\dot{M} \approx 10^{-4}\text{--}10^{-5} M_{\odot} \text{ yr}^{-1}$, WR stars are expected to inject mechanical energy, and chemically processed material into the local ISM (see the review by Crowther 2007, and references therein). With their inherently hot temperatures, classical WR stars are major sources of hydrogen ionizing photons, while their He II ionizing flux strongly depends on the wind strength and vanishes for more dense winds (e.g. Sander & Vink 2020; Sander et al. 2023; Sixtos et al. 2023). Given the manifold impact of WR stars on their host environment, WR stars are important engines of the cosmic matter cycle, for example in the context of ongoing star and planet formation.

For the one region where we identified a BB (ID 39 or WR1) in its spectrum, we can derive an approximate number of WR stars. For this, we first measured the flux of the broad He II $\lambda 4686$ with a simple Gaussian fitting (see Fig. 9). Similar to the study of Mayya et al. (2020, in NGC 1569), the line of [Fe III] $\lambda 4658$ is also present in emission, but it is well separated from the BB, so there is no need for a de-blending procedure, which was necessary in Gómez-González et al. (2021). Given a distance of 98.62 Mpc, we obtain the luminosity of the He II line, assuming it dominates the BB: $L(\text{He II-broad}) = 7.78 \times 10^{38} \text{ erg s}^{-1}$. We do not detect C IV $\lambda\lambda 5801, 5812$, a.k.a. the ‘red-bump’ (RB), ruling out a large presence of WC or WO-type stars. This also justifies our assignment of the entire fitted flux as that of the broad He II line of $L(\text{He II})$ as WC stars could contribute to the BB with a C III $\lambda 4636$ line, sometimes even exceeding the intensity of He II. However, such BBs tend to display a broader FWHM (see, e.g. Gómez-González et al. 2020) which is not the case for WR1. Thus we conclude that WR1 contains mainly WN stars and calculate the number of a typical Nitrogen-rich late-type WNL star with the expression given by López-Sánchez & Esteban (2010): $L_{\text{WNL}}(\text{He II-broad}) = (-5.430 + 0.812x) \times 10^{36} \text{ erg s}^{-1}$ where x is the O abundance. Using the value obtained by the DM, $x = 8.9$, we get $L_{\text{WNL}}(\text{He II}) = 1.472 \times 10^{36} \text{ erg s}^{-1}$. From the observed $L(\text{He II}) = 7.78 \times 10^{38} \text{ erg s}^{-1}$, we estimate a number of 430 WR stars in this region. The aperture diameter of the extracted spectrum is $D_{\text{aper}} = 2.324 \text{ arcsec}$, which corresponds to a size of 1.1 kpc. Our results are shown in Table 5.

By using fluxes from optical spectrophotometry and distances determined with recently available *Gaia* DR3 parallaxes, Crowther, Rate & Bestenlehner (2023) report line luminosities for MW, Large

Table 5. Observed and derived parameters of WR1.

Parameter	Value
$L(\text{He II})$	$7.78 \pm 0.39 \times 10^{38} \text{ erg s}^{-1}$
$\text{FWHM}(\text{He II})$	12.1 \AA
$\text{EW}(\text{He II})$	1.3 \AA
$L(\text{H } \beta)$	$3.15 \pm 0.05 \times 10^{40} \text{ erg s}^{-1}$
$N_{\text{WNL}} (12 + \log(\frac{\text{O}}{\text{H}}) = 8.9)$	430 ± 20
N_{O7V}	6620 ± 100
WR/O	0.065 ± 0.003

Notes. Assumed values from López-Sánchez & Esteban (2010): $L_{\text{WNL}}(\text{He II}) = 1.80 \times 10^{36} \text{ erg s}^{-1} (12 + \log(\frac{\text{O}}{\text{H}}) = 8.9)$; $L_{\text{O7V}}(\text{H } \beta) = 4.76 \times 10^{36} \text{ erg s}^{-1}$.

Magellanic Clouds (LMC) and Small Magellanic Clouds (SMC) WR stars. Prior to this work, the expression from López-Sánchez & Esteban (2010) was commonly used to quantify the WNL stars required for the observed He II luminosity (e.g. Miralles-Caballero et al. 2016; Mayya et al. 2020) in WR galaxies (defined by Conti 1991). Crowther, Rate & Bestenlehner (2023) provide detailed information for the subtypes of each classification. In their table 2 they report He II luminosities for WN2-5w, WN3-7s, WN6-8, WN9-11, WN5-7h, and Of/WN that go from $0.5\text{--}2 \times 10^{36} \text{ erg s}^{-1}$, with uncertainties of the same order, at MW metallicity. Given the distance of our object and the quality of our spectrum (SNR, spatial resolution), we cannot provide a detailed sub-classification for the WN stars in WR1, since He II is the only broad line detected. However, if we consider the values by Crowther, Rate & Bestenlehner (2023) the number of WN stars in WR1 is the exact value depending on the WN subtype which is in the range between 400 and 1500 WR stars, consistent with the value obtained using the expression from López-Sánchez & Esteban (2010).

We further estimate the number of O-type stars in the H II regions by assuming a ‘typical’ luminosity of $L(\text{H } \beta) = 4.76 \times 10^{36} \text{ erg s}^{-1}$ emitted by O 7V stars (López-Sánchez & Esteban 2010). Considering a derived number of 6620 O-type stars in WR1, we obtain a WR/O-ratio of 0.1, which would be consistent with the time that O-type stars are expected to later spend in their WR phase, namely typically ~ 10 per cent of their lifetime (see Crowther 2007).

4.2 ULX sources

ULXs are point X-ray sources located off-center in their host galaxies and having X-ray luminosities $L_X > 3 \times 10^{39} \text{ erg s}^{-1}$, i.e. exceeding the Eddington luminosity of an accreting black hole with $M_{\bullet} \approx 20 M_{\odot}$ (Kaaret, Feng & Roberts 2017). Most likely, ULXs are binaries consisting of a massive donor star and a neutron star or a few M_{\odot} black hole, accreting supercritically (Stobbart, Roberts & Wilms 2006; Poutanen et al. 2007; Gladstone, Roberts & Done 2009; Sutton, Roberts & Middleton 2013). However, stellar evolutionary models predict that some ULXs indeed may contain black holes with masses $> 10 M_{\odot}$ (e.g. Finke & Razaque 2017; Marchant et al. 2017; Hainich et al. 2018). These ULXs would represent an advanced evolutionary stage of a very massive binary star, and therefore are expected to be associated with young massive clusters. Indeed, it is not uncommon to find ULXs located in the vicinity of massive star clusters (Berghea et al. 2013; Poutanen et al. 2013; Oskinova et al. 2019).

The AM 0644-741 galaxy presents an interesting case for studies of ULXs populations. Nine X-ray sources have been detected in this galaxy (Wolter, Fruscione & Mapelli 2018, see their fig. 1). Among them, one is the nucleus of AM 0644-741, and another one is a

Table 6. X-ray sources and their luminosities reported in AM0644-741 by Wolter, Fruscione & Mapelli (2018), assuming a distance of 91.6 Mpc from NED in 2018; updated values assuming 98.62 Mpc (NED) are shown in parentheses[†] and their nearest H II region analysed in this work^{††}. Except for W3 (nucleus) and W5 (AGN^a), these objects have enough luminosities ($L_X > 1 \times 10^{39}$ erg s⁻¹) to be considered ULX sources.

ID [†]	$L_X[0.5-10 \text{ keV}]^{\dagger}$ ($\times 10^{39}$ erg s ⁻¹)	$L_X[2-10 \text{ keV}]^{\dagger}$ ($\times 10^{39}$ erg s ⁻¹)	Nearest ^{††} H II region	Offset (arcsec)	Offset (pc)
W1	8.0 (9.3)	5.1 (5.9)	WR1*	0.75	358.6
W2	12.6 (14.6)	8.1 (9.4)	ID 13	2.0	956.2
W3	28.6 (33.2)	18.1 (21.0)	AGN ^a
W4	9.8 (11.4)	6.3 (7.3)	ID 92*	1.1	525.9
W5	22.4 (26.0)	14.3 (16.6)	Nucleus
W6	2.1 (2.4)	1.3 (1.5)	ID 158	2.1	1004.1
W7	2.3 (2.7)	1.4 (1.6)	ID 170	1.7	812.8
W8	5.1 (5.9)	3.3 (3.8)	ID 113	2.85	1362.7
W9	8.5 (9.9)	5.4 (6.3)	ID 142*	0.8	382.5

Notes. (a) Heida et al. (2013) and corroborated in this work; (*) probably related with the nearby H II region; projected location <1 arcsec. See text for details.

background AGN (Heida et al. 2013) (see also Appendix B). Seven remaining X-ray sources are ULXs. Three of them (W1, W4, and W9) are located at <1.1 arcsec in projection from star clusters and their H II regions (WR1, 92, and 142). The other three ULXs are also located within the star-forming ring and are likely associated with nearby H II regions. Only one ULX, W8, located in the NE section of the ring, has no obvious optical counterpart H II region or star cluster. The projected separation of the X-ray sources to their nearest H II regions are listed in Table 6.

The ULX W1 is especially interesting since its position coincides with the brightest H II region in its host galaxy surrounding a cluster of WR stars (Fig. 2). Given the age and the mass of the associated star cluster, we tentatively suggest that W1 is powered by the accretion on to a black hole. Several ULXs have been observed in association with He III regions (Pakull & Mirioni 2003). However, not all ULXs are associated with a nebular region (Feng & Soria 2011). For example in the Cartwheel only 10 of the 17 ULX sources have associated He II emission. However, line ratios of commonly observed nebular lines do not show any signature of the ionization by X-ray sources (Mayya et al. 2023). No nebular He II lines are detected in the MUSE spectra of the ULX in AM0644-741. This implies that the presence of a ULX and large numbers of WR stars are not a sufficient condition for producing a He III nebula as discussed recently by e.g. Schaerer, Fragos & Izotov (2019) and Umeda et al. (2022). Given the higher than solar metallicity of AM0644-741, the winds of the WR stars are likely too dense to provide a sufficient budget of He II ionizing photons. Recently, Oskinova & Schaerer (2022) suggested that the lower temperature of superbubbles around lower metallicity star clusters could help to explain the observed prevalence of He III nebulae in low-metallicity galaxies.

Another interesting source is W3, the brightest X-ray source on the FoV of AM0644-741. Heida et al. (2013) identified this object as an AGN due to detecting [Mg II] λ 2798 and C III] λ 1909 with the VLT/FOcal Reducer and low dispersion Spectrograph (FORIS2) observations. In Fig. B1 we show the MUSE spectrum extracted at the position of W3, identified as an H α -emission region in our first SEXTRACTOR catalogue. This mis-identification happened due to the [Mg II] λ 2798 line of the AGN being redshifted precisely to the wavelength of H α , which was the criteria to construct our catalogue. Additionally, we identify [O II] λ 3727 and [Ne III] λ 3869 at a similar redshift of $z \sim 1.4$. Their redshifted wavelength range

was not covered in previous observations. Thus, we independently confirm that W3 is a background AGN at $z \sim 1.4$. On top of the wide emission line, we identify a narrow H α absorption line at the redshift of AM0644-741 ($z \sim 0.022$). We use BPT diagrams to check whether any of the observed lines of regions containing ULX sources require ionization from X-rays.

4.3 BPT diagrams

We use the standard diagnostic diagrams to determine the physical parameters such as the age, ionization parameter ($\log \langle U \rangle$), and gas density ($\log n_H$) for the H II regions in the double ring of AM0644-741. For this purpose we use the photoionization calculations of Xiao, Stanway & Eldridge (2018) which are based on CLOUDY models (Ferland et al. 2017) using single and binary population synthesis models of BPASS (Eldridge et al. 2017). We found that the observed points lie between the calculated values for metallicities $Z = 0.014$ and 0.020. We hence generated a new set of tables corresponding to $Z = 0.017$ by interpolating the fluxes of each nebular line from the $Z = 0.014$ and 0.020 tables. These tables were generated for both single and binary star models.

The EW(H β) is a parameter commonly used as an indicator of the age, whereas [O III] λ 5007/H β , [N II] λ 6583/H α , and [S II] λ 6717 + 6731/H α are sensitive to the ionization state of a starburst region. Flux ratios of the [S II] doublet are sensitive to the n_e of H II regions. We hence compare the observed values of these quantities with the results from photoionization models. In Fig. 10, we plot the [O III] λ 5007/H β line ratio versus EW(H β) on the left and [S II] doublet line ratios versus [S II] λ 6717 + 6731/H α on the right. Errors on observed quantities are plotted in both axis but is noticeable only when it is larger than the symbol size. The three H II regions containing ULX sources, one of which is also a WR source, are shown by large red coloured symbols.

On the left figure, photoionization models are shown for single and binary models with continuous and dashed lines, respectively, at five values of $\log U$ ranging from -3.5 to -1.5 at an interval of 0.5 dex. Along each curve, age of the ionizing cluster changes from 1 to 100 Myr, with the colour of the curve denoting interesting ranges of ages: 1–2.5 Myr (blue), 2.5–5 Myr (cyan), 5–10 Myr (green), 10–20 Myr (yellow), and 20–100 Myr (red). The plotted models correspond to density $\log n_H[\text{cm}^{-3}] = 2$.

On the right figure, we show the binary evolutionary tracks for $\log n_H[\text{cm}^{-3}] = 1.5$ and 2.5. The plotted [S II] doublet ratio becomes insensitive to density for $n_H \lesssim 30 \text{ cm}^{-3}$, whereas the ratio decreases for densities higher than the plotted limit. The Figure illustrates that AM0644-741 regions lie between the two plotted ranges, and hence we take a mean density of $n_H = 100 \text{ cm}^{-3}$.

Binary models at low ionization ($-3.5 < \log U < -3.0$) at ages >5 Myr at n_e of 100 cm^{-3} fit the four plotted quantities simultaneously for the majority of the regions. We derive an age of ~ 6 Myr with or without binary for WR1, which is also a ULX (red asterix), whereas for the other two ULX sources, we derive ages of 10 and 25 Myr, respectively, for ID 92 and ID 142. Only binary models reproduce all the observed quantities for these two ULX sources.

In Fig. 11, we plot the observed H II regions in the three standard BPT diagrams (Baldwin, Phillips & Terlevich 1981): (1) [O III] λ 5007/H β versus [N II] λ 6583/H α , (2) [O III] λ 5007/H β versus [S II] λ 6717 + 6731/H α , and (3) [O III] λ 5007/H β versus [O I] λ 6300/H α line ratios. The same photoionization models that are used in the left-hand panel of Fig. 10 are shown on these diagrams. In addition, we draw the maximal starburst locus of Kewley et al. (2006)

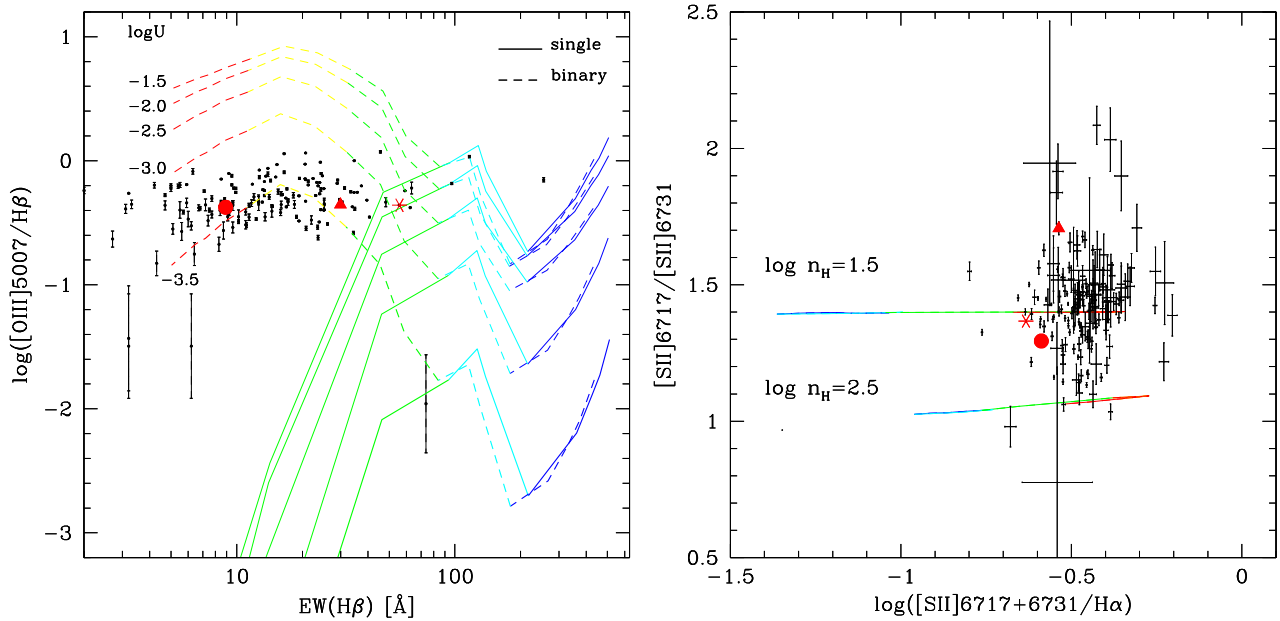


Figure 10. Diagrams for the diagnostic of age and ionization state (left) and density (right) of the H II regions in AM0644-741 (black points with vertical error bars). Red points correspond to special H II regions that have ULX emission (star ID 39 = WR1, triangle ID 92 and circle ID 142). (left) Photoionization model results from Xiao, Stanway & Eldridge (2018) for BPASS single (continuous line) and binary (dashed line) models are plotted at $Z = 0.017$, density $\log n_{\text{H}}[\text{cm}^{-3}] = 2$ for five values of $\log U$, which are identified by the labels. The curves are colour coded to denote the ages: 1–2.5 Myr blue, 2.5–5 Myr cyan, 5–10 Myr green, 10–20 Myr yellow, and 20–100 Myr red. (right) Colour coding of the models is the same as on the left except that only the binary models at $\log U = -3.5$ are shown for two densities which are indicated. Binary low ionization models ($-3.5 < \log U < -3.0$) at ages > 5 Myr at n_e of 100 cm^{-3} fit the four plotted quantities simultaneously for the majority of the regions.

in these plots. As expected, all the H II regions are located in the star-forming zone, including those containing ULX and WRs. In fact, the location of these ULX sources does not differ from that of the rest of the H II regions in these BPT diagrams. The X-ray photons from ULX sources are expected to ionize the neutral medium surrounding the H II regions, creating energetic free electrons in the cold medium. These free electrons collisionally excite oxygen in the cold neutral medium, thus increasing the $[\text{O I}] \lambda 6300/\text{H}\alpha$ ratio to values above those for normal H II regions. (Gúrpide et al. 2022). No such effect is seen, and hence the ULX sources do not contribute in any significant way to the ionization of H II regions. It can be noticed that the same low ionization ($-3.5 < \log U < -3.0$) binary models at ages > 5 Myr and n_e of 100 cm^{-3} that best fit the $[\text{O III}] \lambda 5007/\text{H}\beta$ versus $\text{EW}(\text{H}\beta)$ diagram also fit the plotted quantities simultaneously for the majority of the regions.

As mentioned in the beginning of this section, we have used the results of the photoionization code for $Z = 0.017$. This value corresponds to a gas phase metallicity of $12 + \log(\frac{\text{O}}{\text{H}}) = 8.88$ for dust-free H II regions, whereas it would be 8.65 for dust-to-metal mass ratio of $\xi_d = 0.5$ (Gutkin, Charlot & Bruzual 2016). The inferred gas phase metallicity is closer to the metallicity obtained from the DM rather than the SLM. At lower metallicities, the $[\text{O III}] \lambda 5007/\text{H}\beta$ line ratio requires a higher $\log U$ as compared to the $[\text{N II}] \lambda 6583/\text{H}\alpha$ line ratio.

Single star evolutionary models in BPASS SSP code are able to reproduce the observed values only for regions whose $\text{EW}(\text{H}\beta) > 50 \text{ \AA}$, which corresponds to an age of < 6 Myr. At older ages, line ratios fall rapidly for single star models, whereas the ratios are marginally higher for binary star models. This trend seen in AM0644-741 is similar to the results obtained by Xiao, Stanway & Eldridge (2018) for the sample of H II regions used in their study.

5 DISCUSSION

5.1 Abundances

Until now, there has not been a comprehensive study of the chemical abundances in AM0644-741. The first reports in this regard were made by Higdon, Higdon & Rand (2011), who reported an O abundance of $12 + \log(\frac{\text{O}}{\text{H}}) = 9.1$ for three regions in the ring of AM0644-741. The locations of their slitlets correspond to our objects identified as ID 84 (their slitlet 1); ID 44, 42, 39, and 37 (slitlet 2); and ID 9 (slitlet 3). They used EFOSC2 spectra covering the spectral range from 6200 to 7800 \AA . Given the wavelength range limitations of their spectra, they obtained these values based on $F([\text{N II}])/F(\text{H}\alpha)$ and $F([\text{N II}])/F([\text{S II}])$ relations from Nagao, Maiolino & Marconi (2006). Actually, Higdon, Higdon & Rand (2011) observed the 3500–5500 \AA wavelength range, but due to problems in the reduction process did not use these spectra in their analysis, which is probably the reason why they did not report the WR feature at 4686 \AA in their slitlet 2, where the brightest H II region ID 39 (WR1) is located.

Given the FoV and wavelength range covered by MUSE observations we are able to determine O abundances for 137 regions in the ring of AM0644-741, including those covered by Higdon, Higdon & Rand (2011). We report a median value of $12 + \log(\frac{\text{O}}{\text{H}}) = 8.52$, i.e. slightly subsolar. However, caution should be exercised when comparing this value obtained with the S-calibrator from Pilyugin & Grebel (2016) to those values obtained with different SLM calibrators, as differences of 0.5 dex are common. Conversions between abundances from different SLM calibrators up to the precision of less than 0.1 dex for most of the SLM calibrators do exist (Espinosa-Ponce et al. 2022). We also obtain a slight gradient of $-0.0012 \pm 0.0004 \text{ dex kpc}^{-1}$ among the ellipses 7 and 11. With this estimation, we were able to compare with proper

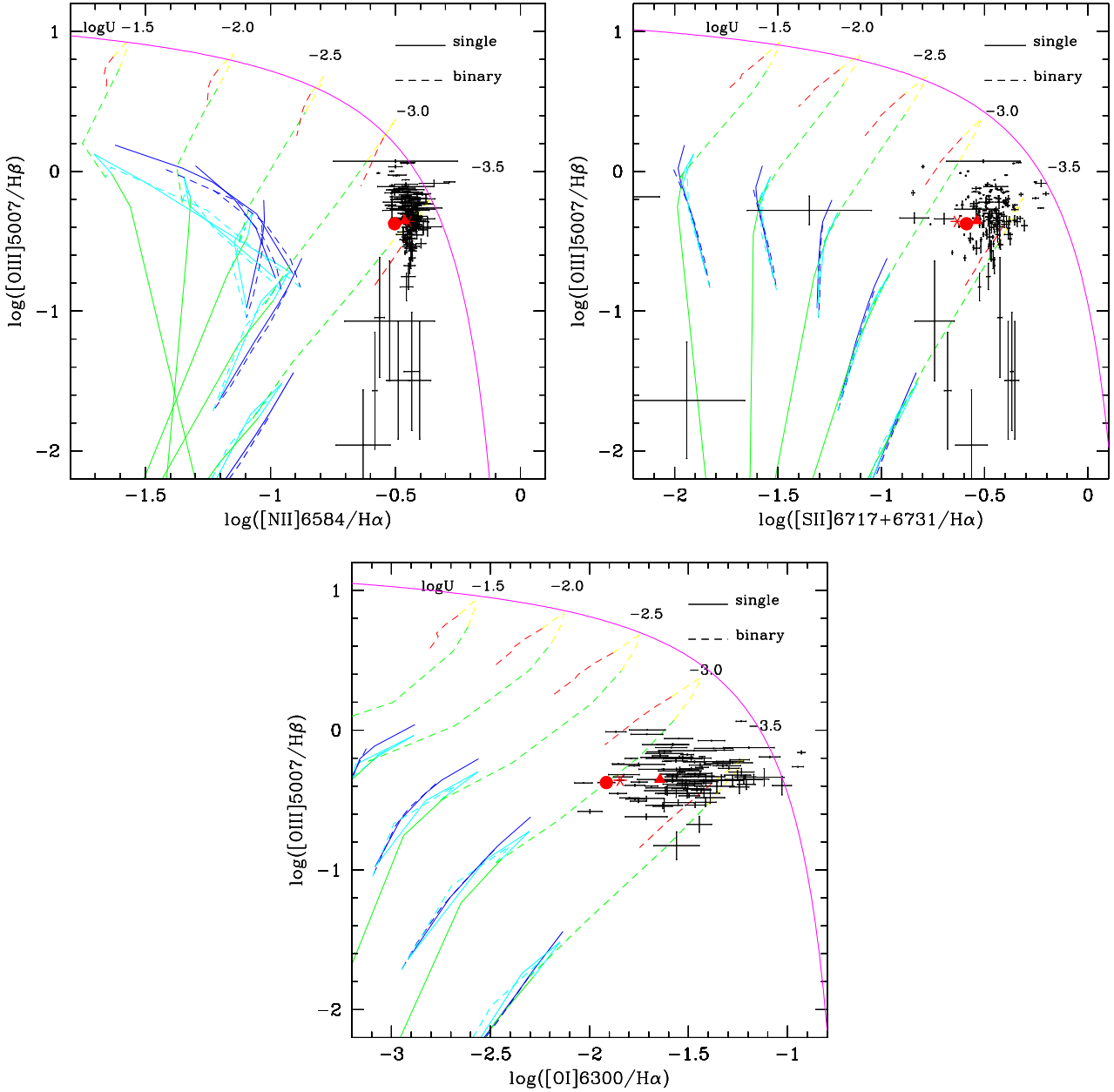


Figure 11. AM 0644-741 H II regions in diagnostic BPT (Baldwin, Phillips & Terlevich 1981) diagrams; (upper left) $[\text{O III}] \lambda 5007/\text{H} \beta$ versus $[\text{N II}] \lambda 6583/\text{H} \alpha$ line ratio; (upper right) $[\text{O III}] \lambda 5007/\text{H} \beta$ versus $[\text{S II}] \lambda 6717 + 6731/\text{H} \alpha$; (bottom) $[\text{O III}] \lambda 5007/\text{H} \beta$ ratio versus $[\text{O I}] \lambda 6300/\text{H} \alpha$. Notations and colour coding of the models and observed points are the same as in Fig. 10. Regions photoionized by stars are expected to lie below the magenta curve defined by Kewley et al. (2006). See text for details.

ionizing models in BPT diagrams and to determine the number of WR stars in WR1. Using the DM, we obtain a supersolar value with $12 + \log(\frac{\text{O}}{\text{H}}) = 8.9 \pm 0.2$, albeit already 0.2 dex lower than previously reported by Higdon, Higdon & Rand (2011).

5.2 Comparison with the cartwheel

AM 0035-335 (the Cartwheel) and AM 0644-741, are probably the most iconic and studied ring-galaxies in the literature. This is in part explained by their striking ring morphology and also their relative proximity, located at 128 and 98.6 Mpc, respectively. In Zaragoza-Cardiel et al. (2022) and Mayya et al. (2023), we started a series of

studies in ring-type galaxies with available MUSE data to analyse the star formation triggered in the ring of these peculiar of galaxies. In Zaragoza-Cardiel et al. (2022), we reported that the H II regions in the ring of the Cartwheel have a median O abundance of $12 + \log(\frac{\text{O}}{\text{H}}) = 8.19 \pm 0.15$, slightly higher than in the SMC. Using the SLM, we here report a median value of $12 + \log(\frac{\text{O}}{\text{H}}) = 8.52$ for AM 0644-741, clearly above Cartwheel and in fact slightly higher than the LMC average (e.g. Toribio San Cipriano et al. 2017).

Comparing the BPT diagram locations of the H II regions studied in this work with those in Cartwheel by Mayya et al. (2023), it is evident that the objects in AM 0644-741 are in a considerably lower state of ionization. Looking at the $[\text{O III}] \lambda 5007/\text{H} \beta$ versus $[\text{N II}] \lambda 6583/\text{H} \alpha$

diagram, for example, the H II regions in Cartwheel are located in the range $0.2 < [\text{O III}] \lambda 5007/\text{H}\beta < 0.9$ and $-1.6[\text{N II}] \lambda 6583/\text{H}\alpha < -1.0$ while regions in AM0644-741 are between $-0.8 < [\text{O III}] \lambda 5007/\text{H}\beta < 0.0$ and $-0.5[\text{N II}] \lambda 6583/\text{H}\alpha < -0.6$. The same can be seen in the other diagrams for $[\text{O III}] \lambda 5007/\text{H}\beta$ versus $[\text{S II}] \lambda 6717 + 6731/\text{H}\alpha$ and $[\text{O III}] \lambda 5007/\text{H}\beta$ versus $[\text{O I}] \lambda 6300/\text{H}\alpha$, our objects are in another zone, at the bottom left of the BPT diagrams relative to the Cartwheel regions, where the ionization parameter can be as high as $\log \langle U \rangle = -2.0$, an order of magnitude higher than in AM0644-741.

Also, Mayya et al. (2023) report the detection of nebular He II $\lambda 4686$ in 32 H II regions in the Cartwheel, with a mean $I(\text{He II } \lambda 4686)/I(\text{H}\beta)$ ratio of 0.010 ± 0.003 . In contrast, we do not detect nebular He II $\lambda 4686$ in the L–S ring. Instead, we detect the broad He II $\lambda 4686$ in the spectrum of a knot of star formation with a luminosity consistent with the presence of at least ~ 430 WR stars. The non-detection of nebular He II $\lambda 4686$ in spite of the detection of a WR feature in the L–S ring is likely due to metallicity difference. At the slightly higher metallicity of L–S ring, it is expected that the atmosphere absorbs the He + ionizing photons more efficiently than at lower metallicity of the Cartwheel.

Like the Cartwheel, AM0644-741 contains a relatively high number of ULXs, conforming the universal scaling of the X-ray luminosity function and star formation rate in galaxies (SFR; Mineo, Gilfanov & Sunyaev 2012). According to Wolter, Fruscione & Mapelli (2018, and references therein), Cartwheel with a SFR of $20 M_{\odot} \text{ yr}^{-1}$ has 15 ULXs and AM0644-741 with an SFR of $11.2 M_{\odot} \text{ yr}^{-1}$ has 7 ULX sources. An anticorrelation between the number of ULXs per host galaxy normalized to the SFR versus the metallicity of the host galaxy is empirically established (Wolter, Fruscione & Mapelli 2018; Lehmer et al. 2021, and references therein). The number of ULXs normalized to the SFR in this galaxy is consistent with the metallicity we report in this work. However, we do not find any evidence of additional ionization by X-ray sources in the H II regions containing ULX sources in AM0644-741, a result which is similar to that found by Mayya et al. (2023) for the Cartwheel H II regions.

6 SUMMARY AND CONCLUDING REMARKS

We have presented an analysis of a sample of H II regions in the star-forming double-ring of the AM0644-741 collisional galaxy using spectra we extracted from available VLT MUSE observations. We constructed a new catalogue of 179 objects following a semi-automatic approach with the standard tool SEXTRACTOR based on the H α emission of these sources. Until now, this is the largest sample of H II regions analysed in this galaxy. This sample could serve as a reference for future studies on star formation triggered in the rings of post-collisional galaxies. After a proper extraction, dereddening, correction for underlying absorption using SSP synthesis models and the flux measurement of all the emission lines present in the spectra, we investigated the chemical abundances and ionization state of these sources. Here, we summarize our findings:

(i) We determined the O abundances for 137 H II regions using the SLM. The rest of the objects did not have all the necessary lines to determine their abundance. We report a median a median O abundance value of $12 + \log \left(\frac{\text{O}}{\text{H}}\right) = 8.52$. This value is between solar ($12 + \log \left(\frac{\text{O}}{\text{H}}\right)_{\odot} = 8.69$; Asplund et al. 2009) and LMC ($12 + \log \left(\frac{\text{O}}{\text{H}}\right) \sim 8.4$; Stasińska et al. 2012, and references therein). A linear fit to the data points among the ellipses including the H II regions of the ring indicates a slight gradient of $-0.0012 \pm 0.0004 \text{ dex kpc}^{-1}$.

There is no indication of an azimuthal gradient. This information was used to select appropriate photoionization models based on the metallicity for further analysis of the physical conditions of H II regions in this galaxy.

(ii) We calculated ionic abundances of He, N, O, and Fe using the DM for the brightest H II region, ID 39. Only this region has all the necessary lines to determine chemical composition via this method. We find values of $12 + \log \left(\frac{\text{He}}{\text{H}}\right) = 10.75 \pm 0.14$; $\log \left(\frac{\text{N}}{\text{O}}\right) = -1.3 \pm 0.2$; $12 + \log \left(\frac{\text{O}}{\text{H}}\right) = 8.9 \pm 0.2$ and $\log \left(\frac{\text{Fe}}{\text{O}}\right) = -2.7 \pm 0.3$. We also determine other physical parameters of the H II regions in the double-ring of this galaxy like flux, SNR and EW of H β , visual extinction A_V and report updated radial velocities.

(iii) We found a WR feature, the BB, in the brightest H II region, naming it WR1. The luminosity of the observed He II $\lambda 4686$ broad line is consistent with the presence of at least ~ 400 WNL WR stars in this knot of massive star formation. We have carried out a careful search for nebular He II $\lambda 4686$ in all the H II regions of this galaxy, but do not detect any narrow He II $\lambda 4686$ in any of the analysed regions.

(iv) We estimate the number of O-type stars in the H II regions assuming a typical luminosity emitted by O7V stars. The $L(\text{H}\beta)$ in WR1 in particular, is consistent with a number of 6620 O-type stars, giving a WR/O ratio of 0.1. This is consistent with the length of the WR phase, ~ 10 per cent of the lifetime of the massive star progenitor.

(v) We observe that the location of at least three of our objects (WR1, 92 and 142) coincide with of one of the ULX sources reported by Wolter, Fruscione & Mapelli (2018) in this galaxy (W1, W4, and W9). The ULXs are related to the star-forming regions in the ring (Wolter, Fruscione & Mapelli 2018). However, we encountered that the exact H II region in our sample is not very clear for half of the ULX sources. Other three ULX sources (W2, W3, and W8) are located a projected distance > 1 arcsec from the nearest H II regions (ID 13, 158, and 113). The analysis of similar ring systems with the presence of ULXs could help to settle their nature and the role they play in the ionization of star-forming regions. However, the optical spectrum does not show line ratios characteristic of ionization by an X-ray source.

(vi) We independently discard the ULX nature of the W3 (Wolter, Fruscione & Mapelli 2018), reporting two additional lines from those reported by Heida et al. (2013) at $z \sim 1.4$ by using novel spectra covering a longer wavelength range. Our result supports the AGN nature of W3. Moreover, we show that its location coincides with a star-like counterpart in optical bands using available HST images.

(vii) By using standard optical diagnostic diagrams with the available emission lines in our spectra: $[\text{O III}] \lambda 5007/\text{H}\beta$ versus $[\text{S II}] \lambda 6717 + 6731/\text{H}\alpha$ and $[\text{O III}] \lambda 5007/\text{H}\beta$ versus $[\text{O I}] \lambda 6300/\text{H}\alpha$, we find that our H II regions are consistent with photoionization by star clusters with ages of 2.5–20 Myr. Comparing the observed line-ratios with single and binary evolution SSP models, we estimate $-3.5 < \log \langle U \rangle < -2.9$ and $\log \langle n_{\text{H}} \rangle$. In three BPT diagrams, a binary population is needed to reproduce the observations.

(viii) In this work we have compared the star-forming regions in the two collisional ring galaxies observed so far with VLT MUSE: the Cartwheel and AM0644-741. They are similar in morphology but turn out to be different in metallicity. The Cartwheel is a relatively metal-poor galaxy (Zaragoza-Cardiel et al. 2022) with a single external ring while AM0644-741 is a double-ring metal-rich galaxy.

(ix) In the Cartwheel, He II nebular has been reported by Mayya et al. (2023). In contrast, AM0644-741 does not show any nebular He II but broad He II in one region. These findings are consistent with the metallicities determined for the two galaxies.

ACKNOWLEDGEMENTS

We thank the anonymous referee for their critical reading and valuable suggestions that improved the presentation of the paper. This work is based on data obtained from the ESO Science Archive Facility, program ID: 106.2155. Observations made with the NASA/ESA *Hubble Space Telescope* were obtained from the data archive at the Space Telescope Science Institute. STScI is operated by the Association of Universities for Research in Astronomy, Inc. under NASA contract NAS 5-26555. This research has made use of the NASA/IPAC Extragalactic Database (NED), which is funded by the National Aeronautics and Space Administration and operated by the California Institute of Technology. VMAGG is funded by the Deutsche Forschungsgemeinschaft (DFG - German Research Foundation), grant number 443790621. YDM thanks CONACYT (Mexico) for the research grant CB-A1-S-25070. AACS is funded by the Deutsche Forschungsgemeinschaft (DFG - German Research Foundation) in the form of an Emmy Noether Research Group – Project-ID 445674056 (SA4064/1-1, PI Sander). AACS further acknowledges supported by funding from the Federal Ministry of Education and Research (BMBF) and the Baden–Württemberg Ministry of Science as part of the Excellence Strategy of the German Federal and State Governments.

DATA AVAILABILITY

Fluxes of the emission lines used in this work are available in its online supplementary material. The reduced fits files on which these data are based will be shared on reasonable request. The ESO datacubes are in the public domain. The link and observation ID are available in the article.

REFERENCES

- Allen D. A., Wright A. E., Goss W. M., 1976, *MNRAS*, 177, 91
 Arellano-Córdova K. Z., Rodríguez M., 2020, *MNRAS*, 497, 672
 Arp H., 1966, *ApJS*, 14, 1
 Arp H. C., Madore B., 1987, *A Catalogue of Southern Peculiar Galaxies and Associations*. Cambridge University Press, Cambridge; New York
 Asplund M., Grevesse N., Sauval A. J., Scott P., 2009, *ARA&A*, 47, 481
 Bacon R. et al., 2010, in McLean I. S., Ramsay S. K., Takami H., eds, Proc. SPIE Conf. Ser. Vol. 7735, *Ground-based and Airborne Instrumentation for Astronomy III*. SPIE, Bellingham, p. 773508
 Baldwin J. A., Phillips M. M., Terlevich R., 1981, *PASP*, 93, 5
 Barrera-Ballesteros J. K. et al., 2020, *MNRAS*, 492, 2651
 Belfiore F. et al., 2022, *A&A*, 659, A26
 Bergeha C. T., Dudik R. P., Tincher J., Winter L. M., 2013, *ApJ*, 776, 100
 Bertin E., Arnouts S., 1996, *A&AS*, 117, 393
 Bittner A. et al., 2019, *A&A*, 628, A117
 Bransford M. A., Appleton P. N., Marston A. P., Charmandaris V., 1998, *AJ*, 116, 2757
 Cardelli J. A., Clayton G. C., Mathis J. S., 1989, *ApJ*, 345, 245
 Chen Y., Bressan A., Girardi L., Marigo P., Kong X., Lanza A., 2015, *MNRAS*, 452, 1068
 Chieffi A., Limongi M., 2013, *ApJ*, 764, 21
 Conti P. S., 1991, *ApJ*, 377, 115
 Crowther P. A., 2007, *ARA&A*, 45, 177
 Crowther P. A., Rate G., Bestenlehner J. M., 2023, *MNRAS*, 521, 585
 Delgado-Inglada G., Mesa-Delgado A., García-Rojas J., Rodríguez M., Esteban C., 2016, *MNRAS*, 456, 3855
 Della Bruna L. et al., 2020, *A&A*, 635, A134
 Dey A. et al., 2019, *AJ*, 157, 168
 Eldridge J. J., Stanway E. R., Xiao L., McClelland L. A. S., Taylor G., Ng M., Greis S. M. L., Bray J. C., 2017, *PASA*, 34, e058
 Espinosa-Ponce C., Sánchez S. F., Morisset C., Barrera-Ballesteros J. K., Galbany L., García-Benito R., Lacerda E. A. D., Mast D., 2020, *MNRAS*, 494, 1622
 Espinosa-Ponce C., Sánchez S. F., Morisset C., Barrera-Ballesteros J. K., Galbany L., García-Benito R., Lacerda E. A. D., Mast D., 2022, *MNRAS*, 512, 3436
 Feng H., Soria R., 2011, *New A Rev.*, 55, 166
 Ferland G. J., Korista K. T., Verner D. A., Ferguson J. W., Kingdon J. B., Verner E. M., 1998, *PASP*, 110, 761
 Ferland G. J. et al., 2017, *RMxAA*, 53, 385
 Few J. M. A., Madore B. F., Arp H. C., 1982, *MNRAS*, 199, 633
 Finke J. D., Razzaque S., 2017, *MNRAS*, 472, 3683
 Fisher K. B., Huchra J. P., Strauss M. A., Davis M., Yahil A., Schlegel D., 1995, *ApJS*, 100, 69
 Garnett D. R., 1990, *ApJ*, 363, 142
 Garnett D. R., 1992, *AJ*, 103, 1330
 Georgy C., Ekström S., Meynet G., Massey P., Levesque E. M., Hirschi R., Eggenberger P., Maeder A., 2012, *A&A*, 542, A29
 Gladstone J. C., Roberts T. P., Done C., 2009, *MNRAS*, 397, 1836
 Gómez-González V. M. A., Mayya Y. D., Rosa-González D., 2016, *MNRAS*, 460, 1555
 Gómez-González V. M. A., Mayya Y. D., Rosa-González D., Rodríguez-Merino L. H., Toalá J. A., Alvarez C., 2020, *MNRAS*, 493, 3879
 Gómez-González V. M. A., Mayya Y. D., Toalá J. A., Arthur S. J., Zaragoza-Cardiel J., Guerrero M. A., 2021, *MNRAS*, 500, 2076
 Gúrpide A., Parra M., Godet O., Contini T., Olive J. F., 2022, *A&A*, 666, A100
 Gutkin J., Charlot S., Bruzual G., 2016, *MNRAS*, 462, 1757
 Hadfield L. J., Crowther P. A., 2006, *MNRAS*, 368, 1822
 Hägele G. F., Pérez-Montero E., Díaz Á. I., Terlevich E., Terlevich R., 2006, *MNRAS*, 372, 293
 Hainich R. et al., 2018, *A&A*, 609, A94
 Heida M., Jonker P. G., Torres M. A. P., Roberts T. P., Miniutti G., Fabian A. C., Ratti E. M., 2013, *MNRAS*, 433, 681
 Higdon J. L., 1995, *ApJ*, 455, 524
 Higdon J. L., Wallin J. F., 1997, *ApJ*, 474, 686
 Higdon J. L., Higdon S. J. U., Rand R. J., 2011, *ApJ*, 739, 97
 Kaaret P., Feng H., Roberts T. P., 2017, *ARA&A*, 55, 303
 Kehrig C. et al., 2013, *MNRAS*, 432, 2731
 Kennicutt Robert C. J., Bresolin F., Garnett D. R., 2003, *ApJ*, 591, 801
 Kewley L. J., Groves B., Kauffmann G., Heckman T., 2006, *MNRAS*, 372, 961
 Kunth D., Sargent W. L. W., 1981, *A&A*, 101, L5
 Lehmer B. D. et al., 2021, *ApJ*, 907, 17
 López-Sánchez Á. R., Esteban C., 2010, *A&A*, 516, A104
 Lugo-Aranda A. Z., Sánchez S. F., Espinosa-Ponce C., López-Cobá C., Galbany L., Barrera-Ballesteros J. K., Sánchez-Menguiano L., Anderson J. P., 2022, *RAS Tech. Instrum.*, 1, 3
 Luridiana V., Morisset C., Shaw R. A., 2015, *A&A*, 573, A42
 Lynds R., Toomre A., 1976, *ApJ*, 209, 382
 Madore B. F., Nelson E., Petrillo K., 2009, *ApJS*, 181, 572
 Magrini L., Gonçalves D. R., Vajgel B., 2017, *MNRAS*, 464, 739
 Mapelli M., Colpi M., Zampieri L., 2009, *MNRAS*, 395, L71
 Marchant P., Langer N., Podsiadlowski P., Tauris T. M., de Mink S., Mandel I., Moriya T. J., 2017, *A&A*, 604, A55
 Marcum P. M., Appleton P. N., Higdon J. L., 1992, *ApJ*, 399, 57
 Massey P., 2003, *ARA&A*, 41, 15
 Mayya Y. D. et al., 2020, *MNRAS*, 498, 1496
 Mayya Y. D., Plat A., Gómez-González V. M. A., Zaragoza-Cardiel J., Charlot S., Bruzual G., 2023, *MNRAS*, 519, 5492
 Mineo S., Gilfanov M., Sunyaev R., 2012, *MNRAS*, 419, 2095
 Miralles-Caballero D. et al., 2016, *A&A*, 592, A105
 Monreal-Ibero A., Walsh J. R., Iglesias-Páramo J., Sandin C., Relaño M., Pérez-Montero E., Vílchez J., 2017, *A&A*, 603, A130
 Nagao T., Maiolino R., Marconi A., 2006, *A&A*, 459, 85
 Oskinova L. M., Schaerer D., 2022, *A&A*, 661, A67
 Oskinova L. M., Bik A., Mas-Hesse J. M., Hayes M., Adamo A., Östlin G., Fürtst F., Otí-Floranes H., 2019, *A&A*, 627, A63

Osterbrock D. E., Ferland G. J., 2006, in Osterbrock D.E., Ferland G.J., eds, *Astrophysics of Gaseous Nebulae and Active Galactic Nuclei*, 2nd. ed, University Science Books, Sausalito, CA

Ott T., 2012, *Astrophysics Source Code Library*, record ascl:1210.019

Pakull M. W., Mirioni L., 2003, in Arthur J., Henney W. J., eds, *Revista Mexicana de Astronomia y Astrofisica Conference Series*, Vol. 15. p. 197

Pilyugin L. S., Grebel E. K., 2016, *MNRAS*, 457, 3678

Poutanen J., Lipunova G., Fabrika S., Butkevich A. G., Abolmasov P., 2007, *MNRAS*, 377, 1187

Poutanen J., Fabrika S., Valeev A. F., Sholukhova O., Greiner J., 2013, *MNRAS*, 432, 506

Renaud F. et al., 2018, *MNRAS*, 473, 585

Rodríguez M., 2002, *A&A*, 389, 556

Sánchez S. F., 2020, *ARA&A*, 58, 99

Sander A. A. C., Vink J. S., 2020, *MNRAS*, 499, 873

Sander A. A. C., Lefever R. R., Poniatowski L. G., Ramachandran V., Sabhahit G. N., Vink J. S., 2023, *A&A*, 670, A83

Schaerer D., Fragos T., Izotov Y. I., 2019, *A&A*, 622, L10

Schlafly E. F., Finkbeiner D. P., 2011, *ApJ*, 737, 103

Sixtos A., Wofford A., Sander A. A. C., Peimbert A., 2023, *MNRAS*, 519, 5656

Stasińska G. et al., 2012, in Stasińska G. et al., eds, *EAS Publications Series* Vol. 54. ESA, Noordwijk, p. 65

Stobbart A. M., Roberts T. P., Wilms J., 2006, *MNRAS*, 368, 397

Sutton A. D., Roberts T. P., Middleton M. J., 2013, *MNRAS*, 435, 1758

Toribio San Cipriano L., García-Rojas J., Esteban C., Bresolin F., Peimbert M., 2016, *MNRAS*, 458, 1866

Toribio San Cipriano L., Domínguez-Guzmán G., Esteban C., García-Rojas J., Mesa-Delgado A., Bresolin F., Rodríguez M., Simón-Díaz S., 2017, *MNRAS*, 467, 3759

Umeda H., Ouchi M., Nakajima K., Isobe Y., Aoyama S., Harikane Y., Ono Y., Matsumoto A., 2022, *ApJ*, 930, 37

Wolter A., Fruscione A., Mapelli M., 2018, *ApJ*, 863, 43

Xiao L., Stanway E. R., Eldridge J. J., 2018, *MNRAS*, 477, 904

Zaragoza-Cardiel J., Gómez-González V. M. A., Mayya D., Ramos-Larios G., 2022, *MNRAS*, 514, 1689

Zurita A., Bresolin F., 2012, *MNRAS*, 427, 1463

APPENDIX A: PHYSICAL PARAMETERS

In Table A1, we report our catalogue the 179 H II regions in the double-ringed AM0644-741 galaxy. Coordinates and physical parameters like the flux $\log(F(H\beta))$, SNR, EW, visual extinction A_V , number of O-type stars N_{O7V} , radial velocity V_{rad} and O abundances $12 + \log(\frac{O}{H})$ are listed. Nine out of the 179 sources with H α emission does not have H β with SNR > 3 and therefore only their coordinates are reported. Deeper observations could improve the SNR of the fainter H II regions for future analysis.

Table A1. Catalogue of the 179 H II regions identified in the double-ringed AM0644-741 galaxy and determined parameters.

ID #	Coordinates (J2000)		H β			A_V [mag]	N_{O7V}	Kinematics V_{rad} [km s ⁻¹]	H97 ID	Abundances $12 + \log(\frac{O}{H})$
	RA [hh:mm:ss]	Dec. [dd:mm:ss]	$\log(F(H\beta))$ [erg cm ⁻² s ⁻¹]	SNR	EW [Å]					
(1)	(2)	(3)	(4)	(5)	(6)	(7)	(8)	(9)	(10)	(11)
1	06:43:05.27	-74:15:16.46	-14.957 ± 0.072	13.8	19.4	0.93 ± 0.12	270	6469.3 ± 6.3	H24	8.50 ± 0.71
2	06:43:04.50	-74:15:16.10	-15.164 ± 0.111	9.0	5.0	0.86 ± 0.16	168	6413.2 ± 29.0	...	8.51 ± 0.90
3	06:43:03.70	-74:15:15.61	-14.728 ± 0.044	22.9	21.3	0.69 ± 0.08	457	6419.6 ± 16.3	...	8.51 ± 0.60
4	06:43:03.13	-74:15:19.27	-15.780 ± 0.227	4.4	20.6	0.09 ± 0.35	41	6260.7 ± 9.3
5	06:43:03.13	-74:15:15.67	-14.431 ± 0.037	26.8	13.9	1.08 ± 0.07	906	6365.0 ± 12.1	H26	8.51 ± 0.40
6	06:43:03.31	-74:15:13.46	-15.032 ± 0.079	12.7	25.2	1.03 ± 0.14	227	6427.8 ± 10.4	...	8.53 ± 0.99
7	06:43:03.88	-74:15:00.47	±
8	06:43:02.45	-74:15:17.31	-15.298 ± 0.139	7.2	16.5	0.82 ± 0.20	123	6287.9 ± 5.2	H26	8.49 ± 0.92
9	06:43:02.57	-74:15:14.22	-14.137 ± 0.037	26.9	23.3	1.62 ± 0.08	1783	6385.0 ± 6.4	H26	8.52 ± 0.72
10	06:43:01.77	-74:15:20.53	±	H27	...
11	06:43:01.92	-74:15:15.73	-14.917 ± 0.087	11.5	20.7	1.17 ± 0.15	296	6307.1 ± 21.0	...	8.49 ± 0.89
12	06:43:02.00	-74:15:12.21	-14.534 ± 0.053	18.8	17.0	1.45 ± 0.10	715	6406.7 ± 7.1
13	06:43:01.57	-74:15:14.22	±
14	06:43:01.70	-74:15:08.94	-15.046 ± 0.060	16.8	14.1	0.75 ± 0.10	220	6402.8 ± 7.5	...	8.52 ± 0.75
15	06:43:01.19	-74:15:12.36	-15.503 ± 0.101	9.9	12.7	0.00 ± 0.00	77	6325.8 ± 5.7	...	8.61 ± 0.44
16	06:43:01.14	-74:15:10.55	-15.020 ± 0.067	14.9	9.2	0.57 ± 0.10	233	6332.1 ± 8.8	...	8.51 ± 0.58
17	06:43:00.96	-74:15:07.40	-14.501 ± 0.036	27.4	15.3	0.97 ± 0.07	771	6371.3 ± 3.5	H29	8.53 ± 0.45
18	06:43:00.35	-74:15:08.07	-14.883 ± 0.085	11.8	7.7	1.16 ± 0.13	320	6315.3 ± 8.3	...	8.51 ± 0.98
19	06:43:00.39	-74:15:06.18	-14.637 ± 0.051	19.7	9.5	1.21 ± 0.08	564	6301.6 ± 1.1	H30	8.52 ± 0.60
20	06:43:00.28	-74:15:05.01	-14.951 ± 0.083	12.0	2.0	0.02 ± 0.10	274	6309.7 ± 13.6	H30	8.53 ± 0.87
21	06:43:00.00	-74:15:09.72	-15.352 ± 0.172	5.8	12.7	0.77 ± 0.33	109	6286.7 ± 2.4	...	8.50 ± 0.89
22	06:42:59.94	-74:15:06.34	-14.682 ± 0.102	9.8	5.0	1.79 ± 0.16	508	6313.4 ± 11.1	H30	8.53 ± 0.91
23	06:42:59.73	-74:15:16.43	±	H28	...
24	06:42:59.45	-74:15:03.06	-14.872 ± 0.074	13.5	5.4	1.08 ± 0.11	328	6299.9 ± 11.2	H31	8.52 ± 0.89
25	06:42:59.97	-74:15:00.76	-14.853 ± 0.048	20.9	13.6	0.69 ± 0.08	343	6315.4 ± 14.4	...	8.50 ± 0.52
26	06:42:59.32	-74:15:01.29	-14.217 ± 0.041	24.4	11.8	1.70 ± 0.08	1483	6298.9 ± 5.5	H31	8.53 ± 0.50
27	06:42:58.97	-74:15:00.04	-14.136 ± 0.023	43.8	24.0	1.43 ± 0.04	1787	6304.7 ± 5.7	H31	8.53 ± 0.47
28	06:42:59.54	-74:14:58.08	-14.753 ± 0.036	27.7	9.9	0.97 ± 0.06	432	6321.4 ± 5.9	H32	8.51 ± 0.58
29	06:42:58.93	-74:14:57.20	-14.198 ± 0.018	54.8	25.1	1.09 ± 0.03	1550	6301.4 ± 3.8	H32	8.53 ± 0.39
30	06:42:58.33	-74:14:54.30	-14.731 ± 0.036	27.7	24.0	0.94 ± 0.06	454	6315.3 ± 4.4	H34	8.51 ± 0.48
31	06:42:59.04	-74:14:54.54	-14.296 ± 0.021	47.0	20.7	1.00 ± 0.04	1237	6333.8 ± 2.7	H33	8.51 ± 0.47
32	06:42:59.57	-74:14:54.84	-13.986 ± 0.012	81.1	59.0	1.12 ± 0.02	2525	6341.9 ± 2.4	H33	8.51 ± 0.40
33	06:42:59.54	-74:14:52.82	-14.182 ± 0.017	58.1	37.3	1.09 ± 0.03	1608	6334.0 ± 2.2	H33	8.52 ± 0.36
34	06:42:58.70	-74:14:52.67	-14.231 ± 0.021	47.8	16.8	1.12 ± 0.04	1436	6333.5 ± 3.1	H34	8.52 ± 0.46

Table A1 – continued

ID #	Coordinates (J2000)		H β		EW [Å]	A_V [mag]	N_{O7V}	Kinematics V_{rad} [km s $^{-1}$]	H97 ID	Abundances 12 + log($\frac{O}{H}$)
	RA [hh:mm:ss]	Dec. [dd:mm:ss]	log(F(H β)) [erg cm $^{-2}$ s $^{-1}$]	SNR						
(1)	(2)	(3)	(4)	(5)	(6)	(7)	(8)	(9)	(10)	(11)
35	06:42:57.50	-74:14:49.45	-15.870 ± 0.238	4.2	20.7	0.00 ± 0.42	33	6410.9 ± 20.3
36	06:42:58.02	-74:14:48.94	-15.010 ± 0.083	12.0	14.5	1.19 ± 0.15	239	6347.8 ± 3.1	H35	8.54 ± 1.11
37	06:42:58.56	-74:14:48.91	-13.872 ± 0.015	65.7	33.9	1.46 ± 0.03	3283	6335.9 ± 5.1	H35	8.56 ± 0.39
38	06:42:57.99	-74:14:44.31	-14.653 ± 0.040	24.7	34.8	0.89 ± 0.08	544	6368.2 ± 6.3	H36	8.55 ± 0.65
39	06:42:58.50	-74:14:44.69	-13.567 ± 0.007	141.2	55.7	1.23 ± 0.01	6626	6349.0 ± 4.0	H36	8.57 ± 0.17
40	06:42:59.16	-74:14:44.93	-14.957 ± 0.043	23.1	13.4	0.73 ± 0.08	270	6334.0 ± 1.8	...	8.54 ± 0.51
41	06:42:57.94	-74:14:42.32	-14.773 ± 0.051	19.5	33.3	1.03 ± 0.07	412	6370.9 ± 9.6	...	8.53 ± 0.62
42	06:42:58.53	-74:14:41.14	-14.122 ± 0.016	63.1	29.8	1.45 ± 0.03	1846	6371.1 ± 4.8	...	8.54 ± 0.34
43	06:42:57.80	-74:14:39.82	-14.872 ± 0.097	10.3	24.7	1.56 ± 0.16	328	6389.1 ± 3.6	...	8.53 ± 0.87
44	06:42:58.73	-74:14:38.07	-14.433 ± 0.020	50.5	25.1	0.79 ± 0.04	902	6387.1 ± 3.7	H37	8.52 ± 0.30
45	06:42:58.64	-74:14:36.73	-14.517 ± 0.023	42.8	19.3	0.86 ± 0.05	743	6402.5 ± 4.3	H37	8.54 ± 0.40
46	06:42:59.26	-74:14:36.89	-15.374 ± 0.085	11.7	7.4	0.53 ± 0.13	103	6371.5 ± 6.1	H37	8.49 ± 1.19
47	06:42:57.66	-74:14:34.98	-15.510 ± 0.303	3.3	5.9	1.17 ± 0.46	76	6414.4 ± 17.0
48	06:42:58.68	-74:14:34.12	-15.171 ± 0.074	13.5	8.4	1.02 ± 0.11	165	6393.5 ± 5.2	...	8.54 ± 1.04
49	06:42:57.71	-74:14:33.88	-15.841 ± 0.233	4.3	3.2	0.20 ± 0.24	35	6415.8 ± 8.1
50	06:42:58.65	-74:14:31.19	-15.280 ± 0.095	10.5	7.2	0.85 ± 0.15	128	6420.5 ± 14.2	...	8.55 ± 1.07
51	06:42:57.71	-74:14:30.30	-15.321 ± 0.115	8.7	9.5	0.84 ± 0.17	117	6426.2 ± 7.1	...	8.52 ± 1.08
52	06:42:58.65	-74:14:28.88	-14.942 ± 0.123	8.1	8.5	1.76 ± 0.22	279	6418.8 ± 10.9	...	8.54 ± 0.88
53	06:43:00.33	-74:14:28.41	-15.712 ± 0.139	7.2	5.1	0.47 ± 0.19	47	6444.9 ± 8.3	...	8.55 ± 1.31
54	06:42:58.86	-74:14:27.02	-14.983 ± 0.075	13.4	8.5	1.34 ± 0.14	254	6412.3 ± 9.9	H38	8.52 ± 0.74
55	06:42:58.90	-74:14:24.82	-14.686 ± 0.048	20.8	17.2	1.32 ± 0.09	504	6443.3 ± 5.4	H38	8.54 ± 0.66
56	06:42:59.25	-74:14:22.03	-15.044 ± 0.052	19.1	13.5	0.90 ± 0.09	221	6464.2 ± 2.9	...	8.53 ± 0.98
57	06:42:59.54	-74:14:19.66	-15.159 ± 0.072	13.8	11.0	1.03 ± 0.12	170	6453.3 ± 2.9	...	8.53 ± 0.88
58	06:43:00.94	-74:14:18.67	-15.709 ± 0.123	8.1	5.6	0.45 ± 0.16	48	6484.1 ± 5.9
59	06:42:58.33	-74:14:18.06	-15.601 ± 0.256	3.9	73.7	0.19 ± 0.69	61	6619.9 ± 10.8	H39	...
60	06:42:59.45	-74:14:17.83	-15.501 ± 0.072	13.8	8.7	0.24 ± 0.11	77	6472.1 ± 4.4	...	8.52 ± 1.33
61	06:42:58.28	-74:14:16.36	±	±	±	±	...	±	H39	...
62	06:42:59.23	-74:14:14.76	-14.839 ± 0.093	10.7	24.3	1.67 ± 0.20	354	6508.8 ± 15.1	H40	8.57 ± 0.99
63	06:42:58.86	-74:14:14.09	-15.241 ± 0.169	5.9	15.5	1.12 ± 0.34	140	6516.7 ± 19.2	H40	8.54 ± 1.11
64	06:42:59.68	-74:14:12.13	-14.802 ± 0.061	16.5	30.4	1.26 ± 0.12	386	6509.5 ± 8.7	H43	8.52 ± 0.76
65	06:43:01.23	-74:14:12.74	±
66	06:42:59.82	-74:14:10.67	-14.597 ± 0.042	23.6	29.6	1.43 ± 0.09	618	6533.6 ± 11.6	H43	8.55 ± 0.70
67	06:43:00.56	-74:14:10.11	-15.432 ± 0.108	9.3	6.2	0.67 ± 0.13	90	6521.8 ± 1.0	...	8.50 ± 1.19
68	06:42:58.36	-74:14:08.15	-15.101 ± 0.333	3.0	45.6	1.74 ± 0.88	194	6602.1 ± 3.7	H42	...
69	06:43:00.31	-74:14:07.09	-15.268 ± 0.092	10.9	16.0	0.90 ± 0.17	132	6538.8 ± 4.6	...	8.50 ± 0.97
70	06:42:58.52	-74:14:03.95	-15.794 ± 0.062	16.1	...	0.52 ± 0.15	39	6621.3 ± 5.9	H44	...
71	06:42:59.00	-74:14:00.72	-15.882 ± 0.087	11.5	...	0.77 ± 0.24	32	6679.3 ± 47.4	H45	...
72	06:43:00.57	-74:14:03.22	-15.113 ± 0.161	6.2	16.0	1.63 ± 0.33	188	6576.5 ± 11.4	H46	8.54 ± 1.17
73	06:43:01.12	-74:14:02.78	-15.056 ± 0.090	11.1	12.6	1.37 ± 0.16	215	6577.6 ± 2.7	H46	8.53 ± 1.01
74	06:43:01.44	-74:14:01.29	-15.249 ± 0.135	7.4	9.6	0.91 ± 0.25	138	6613.6 ± 6.6	H46	8.52 ± 1.18
75	06:43:01.50	-74:14:00.10	-15.344 ± 0.125	8.0	12.6	0.63 ± 0.24	111	6622.4 ± 9.6	H46	...
76	06:43:00.81	-74:13:58.06	-15.575 ± 0.192	5.2	21.3	0.54 ± 0.34	65	6883.1 ± 25.2
77	06:43:00.03	-74:13:56.29	-14.740 ± 0.097	10.3	255.1	0.99 ± 0.20	445	6647.2 ± 2.1	H47	...
78	06:43:02.26	-74:13:57.19	-14.598 ± 0.044	22.8	23.5	1.13 ± 0.08	617	6679.3 ± 21.1	H49	8.54 ± 0.78
79	06:43:02.57	-74:13:55.50	-14.891 ± 0.096	10.4	13.2	1.15 ± 0.19	314	6738.5 ± 41.9	H49	8.54 ± 0.69
80	06:43:03.52	-74:13:55.07	-15.506 ± 0.204	4.9	5.5	0.63 ± 0.33	76	6743.4 ± 9.2
81	06:43:00.77	-74:13:53.53	-15.550 ± 0.278	3.6	31.2	0.74 ± 0.55	69	6714.0 ± 10.0
82	06:43:01.54	-74:13:51.26	-14.820 ± 0.092	10.9	116.5	0.86 ± 0.18	370	6738.8 ± 8.7	H48	8.57 ± 0.84
83	06:43:04.49	-74:13:52.42	-14.889 ± 0.051	19.7	15.9	0.91 ± 0.10	316	6795.9 ± 15.4	H51	8.56 ± 0.79
84	06:43:02.15	-74:13:49.26	-14.445 ± 0.027	36.9	96.7	0.71 ± 0.05	877	6745.7 ± 5.6	H50	8.56 ± 0.58
85	06:43:03.65	-74:13:51.95	-14.967 ± 0.049	20.3	22.4	0.52 ± 0.09	264	6869.4 ± 16.7	H51	8.49 ± 0.61
86	06:43:03.96	-74:13:50.38	-14.661 ± 0.045	22.2	39.5	0.69 ± 0.10	534	6821.5 ± 20.4	H51	8.58 ± 0.52
87	06:43:03.08	-74:13:47.42	-15.318 ± 0.125	8.0	25.2	0.63 ± 0.24	118	6806.1 ± 3.3	...	8.52 ± 1.10
88	06:43:03.18	-74:13:45.67	-15.479 ± 0.172	5.8	18.4	0.57 ± 0.35	81	6807.5 ± 4.6	...	8.51 ± 1.16
89	06:43:03.54	-74:13:46.33	-15.318 ± 0.145	6.9	16.5	0.98 ± 0.27	118	6809.1 ± 5.3	...	8.52 ± 0.88
90	06:43:03.95	-74:13:44.52	-15.466 ± 0.164	6.1	18.2	0.57 ± 0.32	84	6828.1 ± 13.0	...	8.53 ± 0.97
91	06:43:04.43	-74:13:44.07	-15.066 ± 0.092	10.9	23.0	0.75 ± 0.19	210	6833.0 ± 8.0	H52	8.54 ± 0.75
92	06:43:04.80	-74:13:44.17	-14.659 ± 0.049	20.3	29.9	1.05 ± 0.09	536	6836.3 ± 4.3	H52	8.53 ± 0.65
93	06:43:05.01	-74:13:50.39	-15.213 ± 0.064	15.6	17.2	0.34 ± 0.11	150	6869.3 ± 6.5	H53	8.51 ± 0.89
94	06:43:05.48	-74:13:43.90	-15.068 ± 0.097	10.3	15.1	0.96 ± 0.17	209	6847.0 ± 2.9	...	8.56 ± 0.54
95	06:43:05.63	-74:13:51.30	-14.320 ± 0.015	65.9	40.6	0.54 ± 0.03	1170	6852.5 ± 6.9	H53	8.55 ± 0.44
96	06:43:05.94	-74:13:42.63	-15.323 ± 0.189	5.3	6.3	1.05 ± 0.33	116	6908.7 ± 14.4

Table A1 – *continued*

ID #	Coordinates (J2000)		H β		Kinematics			H97	Abundances	
	RA [hh:mm:ss]	Dec. [dd:mm:ss]	$\log(F(H\beta))$ [erg cm ⁻² s ⁻¹]	SNR	EW [Å]	A _v [mag]	N _{O7V}	V _{rad} [km s ⁻¹]	ID	12 + log($\frac{O}{H}$)
(1)	(2)	(3)	(4)	(5)	(6)	(7)	(8)	(9)	(10)	(11)
97	06:43:06.59	-74:13:44.09	-15.461 ± 0.128	7.8	14.3	0.27 ± 0.25	85	6975.0 ± 29.2	...	8.47 ± 0.87
98	06:43:06.64	-74:13:50.90	-15.157 ± 0.068	14.8	12.0	0.53 ± 0.12	170	6878.0 ± 16.3	...	8.55 ± 0.86
99	06:43:07.23	-74:13:49.16	-15.196 ± 0.106	9.4	13.4	0.63 ± 0.21	156	6913.7 ± 10.0	...	8.49 ± 0.83
100	06:43:07.45	-74:13:44.50	-14.781 ± 0.036	27.7	34.6	0.38 ± 0.07	405	6860.6 ± 6.7	H1	8.51 ± 0.52
101	06:43:07.74	-74:13:52.11	-14.457 ± 0.034	29.1	23.6	1.17 ± 0.06	854	6849.6 ± 9.9	...	8.57 ± 0.94
102	06:43:08.89	-74:13:49.28	-15.574 ± 0.152	6.6	5.9	0.29 ± 0.23	65	6934.2 ± 14.0	...	8.49 ± 0.85
103	06:43:08.35	-74:13:53.72	-14.106 ± 0.010	98.6	34.3	0.85 ± 0.02	1915	6860.8 ± 5.1	H2	8.57 ± 0.75
104	06:43:09.27	-74:13:52.38	-15.152 ± 0.068	14.8	8.8	0.56 ± 0.12	172	6931.2 ± 11.5	...	8.52 ± 0.78
105	06:43:09.26	-74:13:53.81	-14.945 ± 0.062	16.1	11.4	0.76 ± 0.12	277	6915.9 ± 7.0	...	8.52 ± 0.79
106	06:43:08.75	-74:13:55.78	-14.450 ± 0.036	27.9	20.8	1.08 ± 0.07	867	6875.5 ± 4.5	H3	8.56 ± 0.75
107	06:43:09.17	-74:13:57.76	-13.973 ± 0.014	71.4	62.4	0.96 ± 0.03	2602	6864.6 ± 3.2	H3	8.63 ± 0.42
108	06:43:10.37	-74:13:56.05	-15.715 ± 0.278	3.6	3.2	0.46 ± 0.40	47	6948.1 ± 13.1
109	06:43:09.64	-74:14:01.53	-14.344 ± 0.022	44.7	24.3	1.19 ± 0.05	1107	6849.1 ± 2.2	H4	8.57 ± 0.50
110	06:43:09.89	-74:14:02.83	-14.381 ± 0.020	50.3	23.9	0.98 ± 0.03	1017	6838.6 ± 11.4	H4	8.54 ± 0.49
111	06:43:11.07	-74:14:01.87	-14.834 ± 0.036	27.9	19.3	0.86 ± 0.06	358	6863.8 ± 4.2	H5	8.52 ± 0.53
112	06:43:11.27	-74:14:04.04	-15.175 ± 0.072	13.9	9.9	0.88 ± 0.11	163	6871.6 ± 18.4	H5	8.53 ± 0.71
113	06:43:10.01	-74:14:05.05	-14.645 ± 0.036	28.0	18.8	1.10 ± 0.06	554	6828.9 ± 17.9	...	8.54 ± 0.74
114	06:43:11.36	-74:14:08.15	-15.393 ± 0.086	11.6	9.6	0.44 ± 0.15	99	6887.9 ± 9.9	H6	8.47 ± 0.95
115	06:43:11.38	-74:14:10.26	-14.776 ± 0.037	27.1	12.3	0.93 ± 0.07	409	6863.2 ± 3.9	H6	8.50 ± 0.69
116	06:43:10.20	-74:14:11.63	-15.105 ± 0.077	13.0	8.3	1.12 ± 0.13	192	6802.6 ± 14.1	H7	8.51 ± 1.36
117	06:43:11.26	-74:14:12.23	-15.134 ± 0.061	16.3	9.2	0.72 ± 0.10	180	6864.7 ± 5.8	H6	8.51 ± 0.82
118	06:43:11.66	-74:14:12.62	-15.634 ± 0.164	6.1	3.1	0.25 ± 0.22	57	6866.3 ± 3.3	H6	8.47 ± 1.15
119	06:43:13.20	-74:14:13.88	±
120	06:43:10.22	-74:14:14.45	-15.291 ± 0.079	12.7	11.4	0.59 ± 0.12	125	6785.7 ± 12.3	H7	8.53 ± 0.93
121	06:43:10.85	-74:14:16.61	-15.052 ± 0.091	11.0	9.1	1.17 ± 0.16	217	6806.3 ± 34.4	H8	...
122	06:43:11.47	-74:14:18.25	-14.922 ± 0.072	13.8	8.8	1.14 ± 0.12	293	6800.0 ± 3.2	H8	8.51 ± 0.87
123	06:43:10.47	-74:14:18.80	-14.928 ± 0.055	18.3	9.6	1.11 ± 0.09	289	6753.1 ± 10.1	...	8.53 ± 1.15
124	06:43:10.71	-74:14:21.14	-14.824 ± 0.046	21.8	14.5	1.12 ± 0.09	367	6751.8 ± 2.2	...	8.53 ± 0.68
125	06:43:11.21	-74:14:22.14	-15.389 ± 0.130	7.7	4.7	0.93 ± 0.19	100	6784.9 ± 3.1	...	8.50 ± 1.11
126	06:43:09.10	-74:14:22.22	-15.383 ± 0.108	9.3	6.7	0.80 ± 0.19	101	6629.8 ± 12.0	...	8.52 ± 1.00
127	06:43:09.51	-74:14:23.02	-15.266 ± 0.070	14.2	11.0	0.73 ± 0.11	133	6651.6 ± 6.5	...	8.54 ± 1.03
128	06:43:10.63	-74:14:24.05	-15.036 ± 0.053	18.9	9.3	0.95 ± 0.08	225	6714.1 ± 8.8	H9	8.54 ± 0.74
129	06:43:11.51	-74:14:25.67	-15.585 ± 0.096	10.4	2.7	0.39 ± 0.08	64	6802.8 ± 9.7	...	8.50 ± 1.44
130	06:43:11.39	-74:14:28.27	-15.427 ± 0.114	8.8	3.3	0.73 ± 0.12	91	6793.5 ± 6.6	...	8.49 ± 1.09
131	06:43:10.88	-74:14:28.66	-14.788 ± 0.034	29.8	13.1	0.89 ± 0.06	398	6782.9 ± 1.3	H11	8.51 ± 0.49
132	06:43:10.12	-74:14:25.82	-14.719 ± 0.041	24.2	10.2	1.26 ± 0.07	467	6672.7 ± 7.0	H9	8.52 ± 0.83
133	06:43:09.65	-74:14:26.74	-14.925 ± 0.045	22.3	11.1	1.00 ± 0.07	291	6632.6 ± 8.6	H9	8.51 ± 0.89
134	06:43:08.93	-74:14:27.24	-14.351 ± 0.020	50.3	26.1	1.27 ± 0.04	1090	6549.7 ± 2.9	H10	8.53 ± 0.62
135	06:43:08.49	-74:14:24.66	-15.316 ± 0.094	10.6	4.3	0.84 ± 0.15	118	6502.0 ± 20.0
136	06:43:08.33	-74:14:25.13	-15.336 ± 0.101	9.9	6.4	0.96 ± 0.17	113	6500.0 ± 17.8
137	06:43:07.03	-74:14:21.39	-15.841 ± 0.333	3.0	0.6	0.00 ± 0.00	35	6356.4 ± 0.0
138	06:43:06.81	-74:14:24.21	-15.737 ± 0.208	4.8	0.9	0.00 ± 0.13	45	6349.1 ± 12.9
139	06:43:10.65	-74:14:30.53	-14.556 ± 0.021	48.4	16.9	0.81 ± 0.04	680	6777.0 ± 4.5	H11	8.51 ± 0.46
140	06:43:10.55	-74:14:33.01	-14.750 ± 0.028	36.1	14.6	0.69 ± 0.05	435	6751.7 ± 10.1	H12	8.51 ± 0.53
141	06:43:11.11	-74:14:34.57	-14.080 ± 0.014	70.1	34.5	1.22 ± 0.03	2033	6768.7 ± 3.3	H12	8.52 ± 0.28
142	06:43:10.46	-74:14:35.18	-14.437 ± 0.017	57.7	8.9	0.48 ± 0.03	894	6726.6 ± 2.8	H12	8.52 ± 0.25
143	06:43:10.45	-74:14:36.57	-14.554 ± 0.028	36.1	8.7	0.51 ± 0.05	683	6724.7 ± 4.4	H12	8.52 ± 0.46
144	06:43:09.15	-74:14:36.20	-15.564 ± 0.145	6.9	4.2	0.80 ± 0.21	67	6638.5 ± 7.5	...	8.55 ± 0.84
145	06:43:10.29	-74:14:38.75	-15.032 ± 0.050	20.2	5.7	0.65 ± 0.06	227	6726.5 ± 3.1	...	8.52 ± 0.78
146	06:43:09.59	-74:14:39.18	-14.943 ± 0.061	16.4	7.7	1.19 ± 0.09	279	6671.7 ± 6.6	...	8.51 ± 0.97
147	06:43:10.62	-74:14:40.50	-15.291 ± 0.084	11.9	7.1	0.69 ± 0.11	125	6739.5 ± 3.9	...	8.52 ± 0.82
148	06:43:11.23	-74:14:42.04	-14.994 ± 0.046	21.7	24.4	0.75 ± 0.07	248	6825.6 ± 2.5	H13	8.48 ± 0.64
149	06:43:09.57	-74:14:42.33	-15.290 ± 0.078	12.8	6.0	0.80 ± 0.08	125	6686.1 ± 5.3	...	8.51 ± 1.31
150	06:43:08.99	-74:14:42.24	-15.178 ± 0.083	12.1	22.0	0.89 ± 0.13	162	6638.0 ± 0.7	...	8.56 ± 1.14
151	06:43:10.38	-74:14:44.26	-15.211 ± 0.056	17.8	13.4	0.34 ± 0.10	150	6715.3 ± 3.3	H14	8.52 ± 0.43
152	06:43:10.08	-74:14:45.78	-14.701 ± 0.025	39.4	20.6	0.54 ± 0.04	487	6703.9 ± 3.5	H14	8.52 ± 0.36
153	06:43:10.87	-74:14:48.93	-15.469 ± 0.161	6.2	16.2	0.70 ± 0.29	83	6767.9 ± 4.1	...	8.46 ± 1.04
154	06:43:10.07	-74:14:48.56	-15.321 ± 0.071	14.1	4.7	0.33 ± 0.10	117	6716.6 ± 4.6	H16	8.52 ± 0.68
155	06:43:09.90	-74:14:50.19	-15.251 ± 0.069	14.5	7.5	0.44 ± 0.12	137	6712.7 ± 14.3	H16	8.50 ± 0.74
156	06:43:09.46	-74:14:50.27	-15.161 ± 0.072	13.8	9.2	0.67 ± 0.12	169	6676.4 ± 12.3	H16	8.51 ± 0.73
157	06:43:09.14	-74:14:51.11	-15.411 ± 0.122	8.2	11.7	0.63 ± 0.23	95	6666.8 ± 1.2	...	8.54 ± 0.93
158	06:43:07.01	-74:14:49.01	±

Table A1 – *continued*

ID #	Coordinates (J2000)		H β		EW [Å]	A _v [mag]	N _{O7V}	Kinematics V _{rad} [km s ⁻¹]	H97 ID	Abundances 12 + log($\frac{O}{H}$)
	RA [hh:mm:ss]	Dec. [dd:mm:ss]	log(F(H β)) [erg cm ⁻² s ⁻¹]	SNR						
(1)	(2)	(3)	(4)	(5)	(6)	(7)	(8)	(9)	(10)	(11)
159	06:43:10.42	-74:14:52.64	-15.705 ± 0.196	5.1	48.2	0.39 ± 0.33	48	6732.7 ± 9.9
160	06:43:11.05	-74:14:54.43	-15.771 ± 0.068	14.8	...	1.00 ± 0.17	41	6790.4 ± 3.0	H17	...
161	06:43:11.93	-74:14:54.83	-15.868 ± 0.083	12.1	...	0.62 ± 0.25	33	6839.9 ± 21.5	H15	...
162	06:43:09.31	-74:14:54.65	-14.945 ± 0.049	20.6	9.7	0.78 ± 0.08	277	6673.6 ± 3.4	H18	8.50 ± 0.69
163	06:43:08.90	-74:14:55.48	-15.356 ± 0.093	10.8	6.8	0.61 ± 0.15	108	6652.9 ± 9.2	H18	8.52 ± 0.82
164	06:43:10.59	-74:14:56.96	-15.787 ± 0.037	27.3	...	0.57 ± 0.09	40	6784.8 ± 13.6	H17	...
165	06:43:11.62	-74:14:57.36	-15.797 ± 0.111	9.0	...	1.42 ± 0.32	39	6822.5 ± 67.8
166	06:43:10.32	-74:14:58.35	-15.947 ± 0.046	21.9	...	0.40 ± 0.10	28	6769.8 ± 18.8	H19	...
167	06:43:09.21	-74:14:58.00	-15.703 ± 0.147	6.8	10.2	0.39 ± 0.21	48	6680.2 ± 8.1
168	06:43:08.71	-74:14:58.70	-15.927 ± 0.182	5.5	5.5	0.18 ± 0.25	29	6622.8 ± 14.9	...	8.52 ± 0.87
169	06:43:10.23	-74:15:01.30	-15.507 ± 0.175	5.7	...	2.57 ± 0.54	76	6724.4 ± 5.9	H19	...
170	06:43:07.46	-74:15:03.44	-16.011 ± 0.313	3.2	3.2	0.00 ± 0.42	24	6586.9 ± 22.4	H21	...
171	06:43:07.91	-74:15:05.86	±	H21	...
172	06:43:09.05	-74:15:06.92	-14.607 ± 0.026	38.4	24.2	0.56 ± 0.03	604	6680.3 ± 7.3	H20	8.49 ± 0.71
173	06:43:09.73	-74:15:06.99	-15.284 ± 0.097	10.3	35.7	0.33 ± 0.12	127	6679.4 ± 10.4	H20	8.49 ± 0.71
174	06:43:09.41	-74:15:08.33	-14.885 ± 0.032	30.9	29.0	0.31 ± 0.04	319	6682.4 ± 1.5	H20	8.49 ± 0.70
175	06:43:09.00	-74:15:09.43	-15.273 ± 0.079	12.7	23.6	0.16 ± 0.14	130	6671.9 ± 6.4	H20	8.48 ± 0.58
176	06:43:08.61	-74:15:10.78	-15.542 ± 0.213	4.7	63.3	0.38 ± 0.33	70	6650.9 ± 8.5
177	06:43:08.69	-74:15:12.43	-15.692 ± 0.323	3.1	28.9	0.61 ± 0.36	50	6638.4 ± 13.7
178	06:43:06.45	-74:15:07.96	-15.543 ± 0.196	5.1	6.2	0.76 ± 0.28	70	6520.4 ± 3.5	H22	...
179	06:43:05.64	-74:15:09.09	-15.036 ± 0.227	4.4	13.9	1.86 ± 0.45	225	6476.2 ± 16.7	H23	8.51 ± 1.35

Note. (1) H II region ID in this work; (2,3) location: right ascension (RA) and declination (Dec.) (J2000); (4) Flux of the H β emission line log(F(H β)) [erg cm⁻² s⁻¹]; (5) signal-to-noise ratio of H β ; (6) equivalent width of H β [Å]; (7) Visual extinction [mag]; (8) derived number of O-type stars; (9) radial velocity [km s⁻¹]; (10) cross ID with Higdon & Wallin (1997); (11) O abundances with the SLM.

APPENDIX B: AGN CONFIRMATION

In Fig. B1, we show the MUSE spectrum of a ‘false’ H II region candidate in the AM0644-741 galaxy. The location of this QSO is indicated in Fig. 1 by a red circle labeled as the X-ray source W3 (Wolter, Fruscione & Mapelli 2018). The spectrum contains

information from astronomical objects at different distances, such as the H α line in absorption at the redshift of AM0644-741. We detected two emission lines of [O II] λ 3727 and [Ne III] λ 3869 at $z \sim 1.4$, confirming its AGN nature, as first reported by Heida et al. (2013).

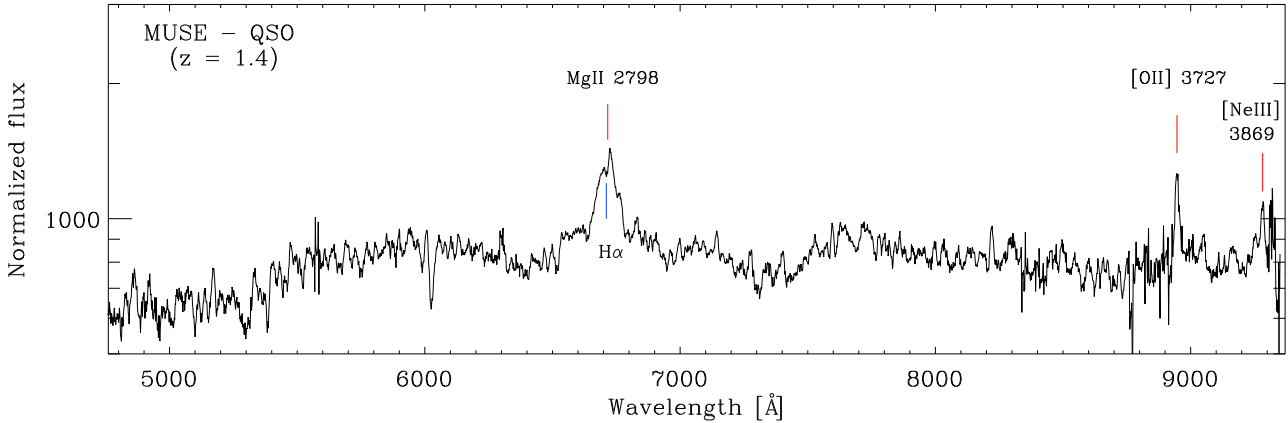


Figure B1. MUSE spectrum of a ‘false’ H II region candidate in the AM0644-741 galaxy. Three emission lines are identified at $z \sim 1.4$ and are indicated above the continuum (red line). The false H α corresponds to [Mg II] λ 2798 (Heida et al. 2013). Although, on top of the wide emission line we do identified the narrow H α line in absorption corresponding to the redshift of AM0644-741 ($z \sim 0.022$). Additionally to Heida et al. (2013), we identified [O II] λ 3727 and [Ne III] λ 3869. Flux is shown normalized to 10^{-20} erg cm⁻² s⁻¹ Å⁻¹.

This paper has been typeset from a \LaTeX file prepared by the author.